Redox Biology 63 (2023) 102735

Contents lists available at ScienceDirect

Redox Biology

journal homepage: www.elsevier.com/locate/redox

TXNIP contributes to induction of pro-inflammatory phenotype and caspase-3 activation in astrocytes during Alzheimer's diseases

Junhyung Kim [a], Jaejoon Lim [b], Ik Dong Yoo [c], Samel Park [d,**], Jong-Seok Moon [a,*]

[a] Department of Integrated Biomedical Science, Soonchunhyang Institute of Medi-bio Science (SIMS), Soonchunhyang University, Cheonan, 31151, Chungcheongnam-do, South Korea
[b] Bundang CHA Medical Center, Department of Neurosurgery, CHA University, Yatap-dong 59, Seong-nam, 13496, South Korea
[c] Department of Nuclear Medicine, Soonchunhyang University Hospital Cheonan, Cheonan, 31151, Chungcheongnam-do, South Korea
[d] Department of Internal Medicine, Soonchunhyang University Hospital Cheonan, Cheonan, 31151, Chungcheongnam-do, South Korea

ARTICLE INFO

Keywords:
TXNIP
Astrocytes
Inflammation
Mitochondrial oxidative stress
Caspase-3
Alzheimer's disease

ABSTRACT

Neuroinflammation and oxidative stress have been implicated in the pathogenesis of Alzheimer's disease (AD). Neuroinflammation and oxidative stress are associated with neuronal death in AD. Astrocytes are linked to neuroinflammation during AD. Astrocytes are important contributors to AD progression. Although the role of thioredoxin-interacting protein (TXNIP) has been identified in inflammation and oxidative stress, the mechanism by which TXNIP regulates inflammation and oxidative stress in astrocytes during AD remains unclear. In the present study, we found that TXNIP gene levels were elevated in cerebral cortex of patients with AD. The protein levels of TXNIP were elevated in GFAP-positive astrocytes of cerebral cortex from patients with AD and APP/PS1 double-transgenic mouse model of AD. Our results showed that TXNIP increased expression of genes related to pro-inflammatory reactive astrocytes and pro-inflammatory cytokines and chemokines in human astrocytes. Moreover, TXNIP increased production of pro-inflammatory cytokines and chemokines in human astrocytes. TXNIP induced activation of NK-kB signaling and over-production of mitochondrial reactive oxygen species (mtROS) in human astrocytes. TXNIP also induced mitochondrial oxidative stress by reduction of mitochondrial respiration and ATP production in human astrocytes. Furthermore, elevated TXNIP levels are correlated with caspase-3 activation of GFAP-positive astrocytes in patients with AD and mouse AD. TXNIP induced mitochondria-dependent apoptosis via caspase-9 and caspase-3 activation in human astrocytes. These results suggest that TXNIP contributes to induction of pro-inflammatory phenotype and caspase-3 activation in astrocytes during AD.

1. Introduction

Alzheimer's disease (AD) is a progressive neurodegenerative disease and the most common type of dementia characterized by memory loss and cognitive dysfunction [1]. Neuroinflammation is also linked to the pathogenesis of AD [2]. Neuroinflammation is implicated in the accumulation of amyloid-β (Aβ) and the formation of neurofibrillary tangles (NFTs), an aggregation of hyperphosphorylated tau protein, during AD [3,4]. Oxidative stress is a critical factor in the initiation and progression of AD [5–7]. Oxidative stress is induced by imbalance in the redox state. It involves over-production of reactive oxygen species (ROS) or dysfunction of the antioxidant system with an imbalance of Ca^{2+} homeostasis [8,9]. Both neuroinflammation and oxidative stress are associated with neuronal cell death during AD [2,6,7].

Astrocytes are the most abundant cell type in the central nervous system (CNS) [10,11]. Astrocytes are responsible for homeostasis, nutrition, and protection of the CNS. Astrocytes play important roles in synapse formation and function, control of neurotransmitters release and uptake, production of trophic factors, and control of neuronal survival [12,13]. In neurodegenerative diseases, loss of normal supportive function in astrocytes has been implicated in neuronal death [14,15]. Previously, we have shown that impairment of astrocytes is elevated in brain of patients with AD [16]. Astrocytes are important regulators of innate and adaptive immune responses in injured CNS [17–19]. In

* Corresponding author. Department of Integrated Biomedical Science, Soonchunhyang Institute of Medi-bio Science (SIMS), Soonchunhyang University, Cheonan, Chungcheongnam-do, South Korea.
** Corresponding author.
E-mail addresses: samelpark17@schmc.ac.kr (S. Park), jongseok81@sch.ac.kr (J.-S. Moon).

https://doi.org/10.1016/j.redox.2023.102735
Received 21 April 2023; Accepted 5 May 2023
Available online 6 May 2023

various pathological conditions, astrocytes can be changed to reactive astrocytes with morphological, molecular, and functional changes [20,21]. Reactive astrocytes exacerbate neuropathology and neurodegeneration under neurodegenerative diseases and neurotoxic conditions [22]. As the concept of astrocyte polarization, reactive astrocytes can convert either into the pro-inflammatory, neurotoxic A1 phenotype or the anti-inflammatory, neuroprotective A2 phenotype [23,24]. The elevation of genes related to pro-inflammatory phenotype including serpin family G member 1 (SERPING1) and proteasome subunit beta type-8 (PSMB8) in reactive astrocytes was reported from the transcriptome analysis from mouse models of brain injury [23,24]. The number of reactive astrocytes, which are expressed markers such as glial fibrillary acidic protein (GFAP) [23,24], is increased in neurodegenerative diseases including AD [25]. The mechanisms involved in the regulation for induction of pro-inflammatory reactive astrocytes during AD were incompletely understood.

Mitochondria in astrocytes regulate brain bioenergetics, neurotransmission, and redox balance [25,26]. As major causes of oxidative stress, mitochondrial dysfunction and damage are prominent and early features of AD [27]. The levels of mitochondrial genes in Complex I of electron transport chain (ETC) are decreased in brains of human AD [28]. Mitochondria are the major source of oxidative stress by producing ROS via electron leakage in ETC including Complex I (NADH:ubiquinone oxidoreductase), Complex II (succinate dehydrogenase), Complex III (coenzyme Q:cytochrome *c* reductase), Complex IV (cytochrome *c* oxidase), and Complex V (ATP synthase) [29]. Inhibition of mitochondrial respiration and ETC activity can lead to mitochondrial oxidative stress via the production of mitochondrial reactive oxygen species (mtROS) [29,30]. mtROS can oxidize mitochondrial glutathione (GSH), which leads to the loss of intramitochondrial redox homeostasis and irreversible oxidative modifications of mitochondrial DNA [31]. In the immune response, mtROS can induce pro-inflammatory signaling such as NF-κB activation [32,33]. Excessive production of mtROS also can induce mitochondria-dependent apoptosis through caspase-9 and caspase-3 activation [34].

Thioredoxin-interacting protein (TXNIP), an important regulator in redox homeostasis, has multiple functions [35–39]. TXNIP can bind to thioredoxin 1 and 2 (TRX1 and TRX2) and inhibit the activity of TRX1 and TRX2, which are antioxidant enzymes that protect against oxidative stress and control ROS. TXNIP can increase the production of ROS and oxidative stress, resulting in cellular apoptosis [35–37]. TXNIP can also induce destructive inflammation [38,39]. Since TXNIP has been linked to inflammation and apoptosis, the role of TXNIP has been identified in various diseases, including type 2 diabetes, atherosclerosis, and myocardial ischemia [38,39]. Recent studies have shown that the levels of TXNIP are increased in both human AD and AD transgenic mice models [40,41]. However, mechanisms by which TXNIP regulates pro-inflammatory phenotype and caspase activation of astrocytes in AD remain unclear.

Here, our results showed that TXNIP levels were elevated in GFAP-positive astrocytes of patients with AD or mouse AD. We found that the elevation of TXNIP increased expression of genes related to pro-inflammatory phenotype, pro-inflammatory cytokines, and chemokines in human astrocytes. TXNIP also increased production of pro-inflammatory cytokines and chemokines and decreased production of growth factors and neurotropic factors in human astrocytes. Moreover, TXNIP induced activation of NF-kB signaling and production of mtROS in human astrocytes. TXNIP also induced mitochondrial oxidative stress by reduction of mitochondrial respiration and ATP production in human astrocytes. Furthermore, high levels of TXNIP are correlated with caspase-3 activation in GFAP-positive astrocytes of patients with AD and mouse AD. TXNIP induced caspase-3 activation and mitochondria-dependent apoptosis in human astrocytes. Our results suggest that TXNIP contributes to induction of pro-inflammatory phenotype and caspase-3 activation in astrocytes during AD.

2. Materials and methods

2.1. Human subject study

A human subject study was conducted in accordance with the Helsinki Declaration. The study protocol was approved by the Institutional Review Board of Soonchunhyang University Hospital Cheonan (SCHCA 2020-03-030-001). A total of 12 paraffin embedded cerebral cortex brain tissues including frontal cortex, occipital cortex, temporal cortex, and parietal cortex from three donors with AD were obtained from the Netherlands Brain Bank. A total of 6 paraffin embedded adult normal brain tissues from six donors including frontal cortex (NBP2-77761), occipital cortex (NBP2-77766), temporal cortex (NBP2-77774) and parietal cortex (NBP2-77769) were obtained from Novus Biologicals (Minneapolis, MN, USA). For immunofluorescence analysis and nanostring nCounter gene expression analysis, cerebral cortex brain tissues including temporal cortex region from patients with AD (AD) and non-AD (normal) were analyzed (Table S1).

2.2. APP/PS1 mouse model of AD

APP/PS1 double-transgenic mice (Stock no. 34829-JAX, B6; C3-Tg (APPswe, PSEN1dE9) 85Dbo/Mmjax) were obtained from the Jackson Laboratory (Bar Harbor, ME USA). APP/PS1 double-transgenic mouse model of Alzheimer's disease (AD) is known to overexpress mutated forms of the genes for human amyloid precursor protein (APP) and presenilin 1 (PS1). APP/PS1 double-transgenic mice (male, 12 months old, n = 5) and C57BL/6 mice (male, 12 months old, n = 5) were used. The brain sections are collected at the critical section according to the mouse brain atlas at bregma (−2.46 to −1.94 mm) for the cortex region at every 4 μm by coronal sections [42]. All mouse experimental protocols were approved by the Institutional Animal Care and Use Committee of Soonchunhyang University (SCH22-0113).

2.3. Reagents and antibodies

The following antibodies were used: monoclonal rabbit anti-TXNIP (#14715, Cell signaling technology, Danvers, MA, USA), monoclonal mouse anti-TXNIP (NBP1-54578, Novus Biologicals, Centennial, CO, USA), monoclonal mouse anti-OXPHOS complex antibody (ab110413, Abcam, Cambridge, UK), monoclonal rabbit anti-cleaved caspase 3 (#9661, Cell signaling technology), monoclonal mouse anti-GFAP (#3670, Cell signaling technology), monoclonal goat anti-GFAP (ab302644, Abcam), polyclonal rabbit anti-Tomm20 antibody (sc-17764, Santa Cruz Biotechnology, Dallas, TX, USA), monoclonal rabbit anti–NF–κB p65 (D14E12) (#8242, Cell signaling technology), monoclonal rabbit anti-phospho–NF–κB p65 (Ser536) (93H1) (#3033, Cell signaling technology), monoclonal rabbit anti-NRF2 antibody (#12721, Cell signaling technology), polyclonal rabbit Histone H3 antibody (#9715, Cell signaling technology), and monoclonal mouse anti-β-actin (A5316, Sigma-Aldrich, St. Louis, MO, USA). Fluoroshield™ with DAPI (F6057, Sigma-Aldrich) was used for nuclear staining and mounting. Sections were mounted onto gelatin-coated slides with Canada Balsam (Wako, Tokyo, Japan) following dehydration.

2.4. Human astrocytes

Human astrocytes N7805100 and #1800 were obtained from Thermo Fisher Scientific (Waltham, MA, USA) and ScienCell Research Laboratories (Carlsbad, CA, USA), respectively. Human astrocytes are normal human cells derived from human brain tissues. Human astrocytes were cultured in Gibco™ Astrocyte Medium containing N-2 Supplement, Dulbecco's Modified Eagle Medium (DMEM), 10% (vol/vol) One Shot™ Fetal Bovine Serum (FBS), 100 units/ml penicillin, and 100 mg/ml streptomycin (A1261301, Thermo Fisher Scientific). For overexpression of human TXNIP, human astrocytes were seeded and

transduced with pCMV6-AC-GFP construct of human TXNIP (NM_006472) as TXNIP over-expressed astrocytes (TXNIP over-expressed cells) (RG210804, Origene, Rockville, MD, USA) or pCMV6-AC-GFP vector (PS100010, Origene) as the control astrocytes (the control cells) using lipofectamine LTX with Plus reagent (15338100, Thermo Fisher Scientific) according to the manufacturer's instructions. Cells were cultured after transduction and incubated for 24 h or 48 h before analysis. Treatment of only lipofectamine LTX and Plus reagent did not affect to cellular morphology and condition in human astrocytes. The efficiency of TXNIP over-expression was 70–80% (number of GFP expressing cells/total number of cells) in cells using measurement by the inherent GFP fluorescence with pCMV6-AC-GFP construct of human TXNIP. Cellular morphology and GFP fluorescence were analyzed by EVOS M5000 Imaging System (Thermo Fisher Scientific) according to the manufacturer's instructions.

2.5. Immunofluorescence analysis

For immunofluorescence analysis, brain tissues were sectioned from paraffin embedded tissue blocks at a thickness of 4 μm. Sections were permeabilized in 0.5% Triton-X (T8787, Sigma-Aldrich) and blocked with CAS-Block™ Histochemical Reagent (008120, Thermo Fisher Scientific). Sections were incubated for 16 h at 4 °C with the following antibodies: monoclonal rabbit anti-TXNIP (1:100) (#14715, Cell signaling technology), monoclonal mouse anti-GFAP (1:100) (#3670, Cell Signaling Technology), monoclonal mouse anti-TXNIP (NBP1-54578, Novus Biologicals), monoclonal rabbit anti-cleaved caspase 3 (1:100) (#9661, Cell signaling technology), monoclonal goat anti-GFAP (1:100) (ab302644, Abcam), and polyclonal rabbit anti-Tomm20 antibody (1:100) (sc-17764, Santa Cruz Biotechnology). Sections were then incubated with goat anti-rabbit IgG (H + L) Alexa Fluor 488 (1:100) (A11008, Thermo Fisher Scientific), goat anti-mouse IgG H&L Texas Red (1:100) (ab6787, Abcam), goat anti-rabbit IgG (H + L) Cross-Adsorbed, Texas Red (1:100) (T-2767, Thermo Fisher Scientific), goat anti-mouse IgG (H + L) Cross-Adsorbed, Alexa Fluor 488 (1:100) (A-11001, Thermo Fisher Scientific), or donkey anti-goat IgG H&L Alexa Fluor 647 (1:100) (ab150131, Abcam) secondary antibody for 2 h at 25 °C. Fluoroshield™ with DAPI (F6057, Sigma-Aldrich) was used for nuclear staining. Stained brain sections were analyzed with THUNDER Imager Tissue (Leica Microsystems Ltd., Wetzlar, Germany). Stained brain sections were quantified with LAS X image-processing software (Leica Microsystems Ltd.) and ImageJ software v1.52a (Bethesda, MD, USA). Cells were plated onto autoclaved glass coverslips placed in 6-well cell culture plates, fixed with 4% paraformaldehyde (PFA), permeabilized with 0.5% Triton-X (T8787, Sigma-Aldrich), blocked with CAS-Block™ Histochemical Reagent (008120, Thermo Fisher Scientific), and then stained as described above. In the measurement for relative intensity of fluorescence, we measured mean fluorescence intensity (MFI) for individual fluorescent channel (blue, green, purple, or red color) in a region of interest (ROI) from images (total n = 10) per individual subject using ImageJ software v1.52a (Bethesda, MD, USA). Final MFI was calculated by MFI values of an ROI compared to MFI values of Background. After we measured final MFI for each fluorescent channel separately, we quantitated the relative intensity of fluorescence in tissues of patients with AD (AD) compared to tissues of non-AD (normal) as a basal level. To ensure objectivity, all analyses were conducted with blinded conditions by two observers who performed analyses using identical conditions per experiment.

2.6. Mitochondrial respiration activity assay

Human astrocytes (5×10^4 cells/well) were plated into XF96 cell culture microplates (101085-004, Agilent Technologies, Inc., Santa Clara, CA, USA) and treated with indicated compound. Oxygen consumption rate (OCR), a parameter of mitochondrial oxygen consumption and respiration, was measured with Seahorse XF96e bioanalyzer using XF Mito Stress Test Kit (103015-100, Agilent Technologies, Inc.) according to the manufacturer's instructions. OCR levels in cells treated with oligomycin (2 μM), FCCP (5 μM), rotenone (10 μM), and antimycin (10 μM) were monitored and measured.

2.7. Mitochondrial ATP production rate assay

Human astrocytes (5×10^4 cells/well) were plated into XF96 cell culture microplates (101085-004, Agilent Technologies) and treated with indicated compound. Real-Time ATP production rate was measured with Seahorse XF96e bioanalyzer using XF Real-Time ATP Rate Assay Kit (103592-100, Agilent Technologies, Inc.) according to the manufacturer's instructions. OCR levels in cells that were treated with oligomycin (2 μM), rotenone (10 μM), and antimycin (10 μM) were monitored and measured.

2.8. Analysis of fragmented mitochondria by mitochondrial morphology

Human astrocytes (1×10^5 cells) were plated into autoclaved glass coverslips placed in 6-well cell culture plates. Cells were transduced with pCMV6-AC-GFP construct of human TXNIP (NM_006472) (500 ng, RG210804, Origene) or of pCMV6-AC-GFP vector (500 ng, PS100010, Origene). Cells were cultured after transduction and incubated for 48 h before analysis. Cells were fixed with 4% paraformaldehyde (PFA), permeabilized with 0.5% Triton-X (T8787, Sigma-Aldrich), and blocked with CAS-Block™ Histochemical Reagent (008120, Thermo Fisher Scientific). Cells were then incubated with polyclonal rabbit anti-Tomm20 antibody (1:100) (sc-17764, Santa Cruz Biotechnology) for 16 h at 4 °C. Cells were then incubated with goat anti-rabbit IgG (H + L) Alexa Fluor 488 (1:100) (A11008, Thermo Fisher Scientific) secondary antibody for 2 h at 25 °C. Fluoroshield™ with DAPI (F6057, Sigma-Aldrich) was used for nuclear staining. Cells were analyzed with THUNDER Imager Tissue (Leica Microsystems Ltd.). Fragmented mitochondria (shortened, punctate, and rounded shape) were determined by mitochondria morphological analysis. Normal mitochondria were determined based on filamentous shape and thread-like tubular structure. Cells with the majority (>70%) showing fragmented mitochondria were determined as cells with mitochondrial fragmentation.

2.9. 2D and 3D imaging analysis

Human astrocytes (1×10^5 cells) were seeded into FluoroDishTM (FD35-100, World Precision Instruments, Sarasota, FL, USA). Cells were transduced with pCMV6-AC-GFP construct of human TXNIP (NM_006472) (500 ng, RG210804, Origene) or of pCMV6-AC-GFP vector (500 ng, PS100010, Origene). Cells were cultured after transduction and incubated for 24 h before analysis. 2D and 3D images were analyzed with 3D Cell Explorer (NANOLIVE, Ecublens, Switzerland). Images were representative images from a total of 100 cells in 10 individual images per group. The percent of morphological dead cells in a total of 100 cells from 10 individual images per group was calculated.

2.10. Immunoblot analysis

Cells were harvested and lysed with Cell Lysis Buffer II (200 μl) (FNN0021, Thermo Fisher Scientific). Lysates were centrifuged at 15,300×*g* for 10 min at 4 °C and supernatants were obtained. Protein concentrations of supernatants were determined with Bio-Rad Protein Assay Dye Reagent Concentrate (500-0006, Bio-Rad Laboratories, Hercules, CA, USA). Proteins (20 or 30 μg) were electrophoresed on NuPAGE 4%–12% Bis-Tris gels (Thermo Fisher Scientific) and transferred to Protran nitrocellulose membranes (10600001, GE Healthcare Life science, Pittsburgh, PA, USA). Membranes were blocked with 5% (w/v) bovine serum albumin (BSA) (9048-46-8, Santa Cruz Biotechnology) in TBS-T (TBS (170–6435, Bio-Rad Laboratories) and 1% (v/v) Tween-20 (170–6531, Bio-Rad Laboratories)) for 30 min at 25 °C.

Membranes were incubated with primary antibody (1:1000) diluted with 1% (w/v) BSA in TBS-T for 16 h at 4 °C and then incubated with horseradish peroxidase (HRP)-conjugated secondary antibody (goat anti–rabbit IgG–HRP (sc-2004) (1:2500), goat anti–mouse IgG–HRP (sc-2005) (1:2500) or mouse anti-goat IgG-HRP (sc-2354) from Santa Cruz Biotechnology) diluted in TBS-T for 2 h at room temperature. Immunoreactive bands were detected with a SuperSignal West Pico Chemiluminescent Substrate (34078, Thermo Fisher Scientific) using the Kwikquant Imager (Kindle Biosciences, LLC, USA) or X-ray film.

2.11. Mitochondrial ROS production analysis

Mitochondrial ROS levels were measured by MitoSOX™ Mitochondrial Superoxide Indicators (M36008, Thermo Fisher Scientific) staining. Human astrocytes (2×10^5 cells) were plated into 6-well cell culture plates. Cells were transduced with pCMV6-AC-GFP construct of human TXNIP (NM_006472) (500 ng, RG210804, Origene) or pCMV6-AC-GFP vector (500 ng, PS100010, Origene). Cells were cultured after transduction and incubated for 24 h before analysis. Cells were washed with PBS, treated with trypsin, and resuspended in OPTI-MEM (31985070, Thermo Fisher Scientific). Data were acquired with Guava® Muse® Cell Analyzer (Luminex Corporation, Austin, TX, USA) according to the manufacturer's instructions.

2.12. Measurement of GSH, ratio of GSH/GSSG, and GSSG

Human astrocytes (2×10^5 cells) were transduced with pCMV6-AC-GFP construct of human TXNIP (NM_006472) (500 ng, RG210804, Origene) or pCMV6-AC-GFP vector (500 ng, PS100010, Origene). Cells were cultured after transduction and incubated for 48 h before analysis. Glutathione (GSH) in protein lysate (100 μg) of human astrocytes was measured using GSH Assay Kit (Colorimetric) (ab239727, Abcam) following the manufacturer's instructions. The ratio of GSH/oxidized glutathione (GSSG) and GSSG in protein lysates (100 μg) of human astrocytes were measured using GSH + GSSG/GSH Assay Kit (Colorimetric) (ab239709, Abcam) following the manufacturer's instructions. The ratio of GSH/GSSG was determined as the ratio of GSH squared over GSSG and presented as $GSH^2/GSSG$.

2.13. Isolation of nuclear and cytosolic proteins

Nuclear and cytosolic proteins were isolated from human astrocytes using Nuclear/Cytosol Fractionation Kit (ab289882, Abcam) following the manufacturer's instructions. Briefly, human astrocytes (1×10^6 cells in 100 mm cell culture plate) were seeded and transduced with pCMV6-AC-GFP construct of human TXNIP (NM_006472) (3 μg, RG210804, Origene) or pCMV6-AC-GFP vector (3 μg, PS100010, Origene). Cells were cultured after transduction and incubated for 48 h before analysis.

2.14. Measurement of HO-1 levels and activity

Human astrocytes (2×10^5 cells) were transduced with pCMV6-AC-GFP construct of human TXNIP (NM_006472) (500 ng, RG210804, Origene) or pCMV6-AC-GFP vector (500 ng, PS100010, Origene). Cells were cultured after transduction and incubated for 48 h before analysis. Levels of HO-1 in human astrocytes were measured using Heme Oxygenase 1 (HO1) (Human) ELISA Kit (#E4507-100, BioVision, Milpitas, CA, USA) following the manufacturer's instructions. The activity of HO-1 was analyzed by quantifying bilirubin production in human astrocytes using Bilirubin Assay Kit (Total and Direct, Colorimetric) (ab235627, Abcam) following the manufacturer's instructions.

2.15. Measurement of GCLC levels and GCL activity

Human astrocytes (2×10^5 cells) were transduced with pCMV6-AC-GFP construct of human TXNIP (NM_006472) (500 ng, RG210804, Origene) or pCMV6-AC-GFP vector (500 ng, PS100010, Origene). Cells were cultured after transduction and incubated for 48 h before analysis. The levels of glutamate cysteine ligase catalytic subunit (GCLC) in human astrocytes were measured using Human GCLC ELISA Kit (ab233632, Abcam) following the manufacturer's instructions. The activity of GCL in human astrocytes was measured using glutamate cysteine ligase (GCL) Assay Kit (MBS9719033, MyBioSource, Inc., San Diego, CA, USA) following the manufacturer's instructions.

2.16. Measurement of caspase-3 and caspase-9 activities

Activities of caspase-3 and caspase-9 in human astrocytes were measured using Caspase-3 Assay Kit (Colorimetric) (ab39401, Abcam) and Caspase-9 Assay Kit (Colorimetric) (ab65608, Abcam) following the manufacturer's instructions. Briefly, human astrocytes (2×10^5 cells in 6-well cell culture plate) were seeded and transduced with pCMV6-AC-GFP construct of human TXNIP (NM_006472) (500 ng, RG210804, Origene) or pCMV6-AC-GFP vector (500 ng, PS100010, Origene). Cells were cultured after transduction and incubated for 48 h before analysis.

2.17. Cell cytotoxicity assay

Cell cytotoxicity was measured using culture medium of human astrocytes with lactate dehydrogenase (LDH) Assay Kit (Cytotoxicity) (ab65393, Abcam) following the manufacturer's instructions. Briefly, human astrocytes (2×10^5 cells in 6-well cell culture plate) were seeded and transduced with pCMV6-AC-GFP construct of human TXNIP (NM_006472) (500 ng, RG210804, Origene) or pCMV6-AC-GFP vector (500 ng, PS100010, Origene). Cells were cultured after transduction and incubated for 48 h before analysis.

2.18. Cytokine and chemokine analysis

Human astrocytes (2×10^5 cells in 6-well cell culture plate) were seeded and transduced with pCMV6-AC-GFP construct of human TXNIP (NM_006472) (500 ng, RG210804, Origene) or pCMV6-AC-GFP vector (500 ng, PS100010, Origene). Cells were cultured after transduction and incubated for 48 h before analysis. Culture media supernatants (800 μl) were used to determine levels of CD147, IL-6, CXCL10, CXCL11, LCN2, MIF, CCL5, and 104 soluble proteins including cytokines, chemokines, and growth factors with Human XL Cytokine Array Kit (ARY022B, R&D systems, Minneapolis, MN, USA) according to the manufacturer's instructions. Culture media supernatants were incubated with four nitrocellulose membranes containing 111 different captured antibodies printed in duplicate for 16 h at 4 °C. Nitrocellulose membranes were incubated with a detection antibody diluted in an assay buffer for 2 h at room temperature and then incubated with streptavidin-horseradish peroxidase (HRP) in an assay buffer for 0.5 h at room temperature. Immunoreactive spots on nitrocellulose membranes were detected with a chemical reagent mix and then exposed to X-ray film. Multiple exposure time were used. Pixel densities from positive signals on developed X-ray films were collected and analyzed using transmission mode scanner and image analysis software (HLImage++ Version 25.0.0r, https://www.wvision.com/QuickSpots.html, Western Vision Software, Salt Lake City, UT, USA).

2.19. RNA extraction and nanostring nCounter gene expression analysis

Total RNA was extracted with Maxwell® RSC RNA FFPE Kit (AS1440, Promega, Madison, WI, USA), Maxwell® RSC simplyRNA tissue kit (AS1340, Promega), or Maxwell® RSC simplyRNA cells kit (AS1390, Promega) with Maxwell® RSC Instrument (AS4500, Promega). Amounts of RNA were measured with QuantiFluor® RNA System (E3310, Promega) using Quantus™ Fluorometer (E6150, Promega). For each sample, 50 ng of total RNA was hybridized for 20 h at 65 °C with probes from the nCounter Human Autoimmune Profiling Panel

containing 750 target genes and 20 reference genes (NanoString Technologies Inc., Seattle, WA, USA). Samples were analyzed using nCounter SPRINT profiler (NanoString Technologies Inc.) according to the manufacturer's instructions. Before differential expression analysis, raw data were normalized using nSOLVER 4.0 (NanoString Technologies Inc.) by performing background subtraction, positive control normalization, and normalization to housekeeping genes. Raw gene expression values were normalized using GeNorm algorithm nCounter Advanced Analysis (Version 2.0.115). Normalized values were transformed to log2 values.

2.20. Cytosolic/mitochondrial fraction and cytochrome c quantification analysis

Cytosolic and mitochondrial faction were isolated from human astrocytes using Mitochondria/Cytosol Fractionation Kit (ab65320, Abcam) following the manufacturer's instructions. Cytochrome *c* levels were measured with Human Cytochrome C ELISA Kit (ab221832, Abcam) following the manufacturer's instructions. Briefly, human astrocytes (1×10^6 cells in 100 mm cell culture plate) were seeded and transduced with pCMV6-AC-GFP construct of human TXNIP (NM_006472) (3 μg, RG210804, Origene) or pCMV6-AC-GFP vector (3 μg, PS100010, Origene). Cells were cultured after transduction and incubated for 48 h before analysis.

2.21. Statistical analysis

Assumptions of normality and homogeneity of variance were assessed. A Shapiro-Wilk test was conducted for normal distribution. Levene's test was conducted for homogeneity of variance. Data are random, independent, and normally distributed with a common variance. All data are presented as mean ± standard deviation (SD) or standard error of the mean (SEM). All statistical analyses were performed using a two-tailed Student's t-test for comparison of two groups and analysis of variance (ANOVA) (with post hoc comparisons using Dunnett's test) using a statistical software package (GraphPad Prism version 8.0, GraphPad Software Inc., San Diego, CA, USA) for comparison of multiple groups. *P*-values of less than 0.05 (*, $p < 0.05$; **, $p < 0.01$; and ***, $p < 0.001$) were considered statistically significant.

3. Results

3.1. The levels of TXNIP are elevated in GFAP-positive astrocytes of cortex from patients with AD

To investigate the role of TXNIP in astrocytes of cerebral cortex regions from patients with AD, we first analyzed TXNIP gene expression levels in cerebral cortex tissues of patients with AD using nanostring nCounter gene expression profiling system (Fig. 1A and Table S1). TXNIP mRNA levels were significantly elevated in cerebral cortex tissues of patients with AD (AD) relative to those in non-AD donor (Normal) (Fig. 1B). Next, we analyzed whether TXNIP protein levels were elevated in astrocytes of cerebral cortex region in brain tissues from patients with AD. TXNIP protein levels in GFAP-positive astrocytes of cerebral cortex tissues from patients with AD or non-AD donor (Normal) were measured using immunofluorescence staining (Fig. 1C and S1). Immunofluorescence staining revealed that the intensity of TXNIP-positive staining in GFAP-positive astrocytes was increased in molecular layer (ML) of the cerebral cortex region of patients with AD (AD) relative to non-AD donor (Normal) (Fig. 1C and D). The number of astrocytes with positive subcellular co-localization between TXNIP and GFAP was significantly increased in patients with AD (AD) (Fig. 1C and E). The number of TXNIP and GFAP-double positive astrocytes was generally higher in each patient with AD (AD) compared to non-AD donor (Normal) (Fig. 1E). These results suggest that TXNIP levels are elevated in GFAP-positive astrocytes of cortex from patients with AD.

3.2. The levels of TXNIP are elevated in GFAP-positive astrocytes of cortex from APP/PS1 mice

Next, we investigated the role of TXNIP in astrocytes of APP/PS1 double-transgenic mouse model of AD. We analyzed whether TXNIP protein levels were elevated in astrocytes of cortex from APP/PS1 mice brains. We measured protein levels of TXNIP in GFAP-positive astrocytes of cortex from APP/PS1 mice or wild-type (WT) mice using immunofluorescence staining (Fig. 2A and S2). The intensity of TXNIP-positive staining in GFAP-positive astrocytes was increased in the cortex region of APP/PS1 mice compared to that in WT mice (Fig. 2A and B). The number of astrocytes with positive subcellular co-localization between TXNIP and GFAP was significantly increased in APP/PS1 mice relative to that in WT mice (Fig. 2A and C). These results suggest that TXNIP levels are elevated in GFAP-positive astrocytes of cortex in APP/PS1 mice.

3.3. TXNIP increases pro-inflammatory phenotype in human astrocytes

To investigate the role of TXNIP in the induction of pro-inflammatory phenotype in astrocytes, we first examined whether the elevation of TXNIP could increase expression of genes related to pro-inflammatory phenotype, pro-inflammatory cytokines, and chemokines in human astrocytes. We analyzed the levels of genes using nCounter gene expression profiling system in TXNIP-over expressed human astrocytes (Fig. 3A). Notably, the mRNA levels of genes related to pro-inflammatory phenotype including SERPING1, PSMB8, human leukocyte antigens (HLA)-A, and HLA-E were significantly increased in TXNIP over-expressed human astrocytes relative to those in the control astrocytes (Fig. 3B). Also, the mRNA levels of C-X-C motif chemokine ligand 10 (CXCL10) gene related to reactive astrocytes were increased by TXNIP over-expression compared to the control. Moreover, the mRNA levels of genes for pro-inflammatory cytokines and chemokines such as interleukin (IL)-1α, IL-1β, IL-6, chemokine (C–C motif) ligand 5 (CCL5), CCL20, CXCL2, and CXCL8 were significantly increased in TXNIP over-expressed human astrocytes compared to those in the control astrocytes (Fig. 3B).

Next, we analyzed whether TXNIP could increase production and secretion of inflammatory cytokines and chemokines in human astrocytes. We measured levels of IL-6, CXCL10, CXCL11, CCL5, lipocalin 2 (LCN2), CD147, macrophage migration inhibitory factor (MIF) and 104 soluble proteins including cytokines, chemokines, growth factors and neurotrophic factors in supernatant from TXNIP-over expressed human astrocytes (Fig. 3C and Table S2). Consistent with expression of genes, the levels of pro-inflammatory cytokines and chemokines such as IL-6, CXCL10, CXCL11, and CCL5 were significantly increased by TXNIP over-expression relative to those in the control (Fig. 3C and D). Additionally, the levels of secretory factors related to reactive astrocytes including LCN2, CD147, and MIF were significantly increased by TXNIP over-expression compared to those in the control (Fig. 3C and D). In contrast, growth factors and neurotrophic factors related to blood vessel formation (angiogenin and vascular endothelial growth factor (VEGF)), and proliferation and differentiation (dickkopf-related protein-1 (Dkk-1), growth/differentiation factor-15 (GDF-15), insulin-like growth factor binding protein (IGFBP)-2, IGFBP-3, osteopontin (OPN), platelet-derived growth factor-AA (PDGF-AA), thrombospondin-1 (TSP-1), and urokinase plasminogen-activator receptor (uPAR)), and other chemokines (CCL2, Pentraxin 3 (PTX3), and CXCL1) levels were significantly decreased by TXNIP over-expression compared to those in the control (Fig. 3C and D). We next investigated the upstream signaling pathway for production of pro-inflammatory cytokines and chemokines by TXNIP over-expression in human astrocytes. Since NF-kB signaling plays a critical role in regulation of pro-inflammatory cytokines and chemokines such as IL-6 and CXCL10, we analyzed whether TXNIP could induce the activation of NF-kB signaling in human astrocytes. Notably, NF-kB phosphorylation levels were significantly increased by TXNIP over-expression relative to the control (Fig. 3E). These results suggest

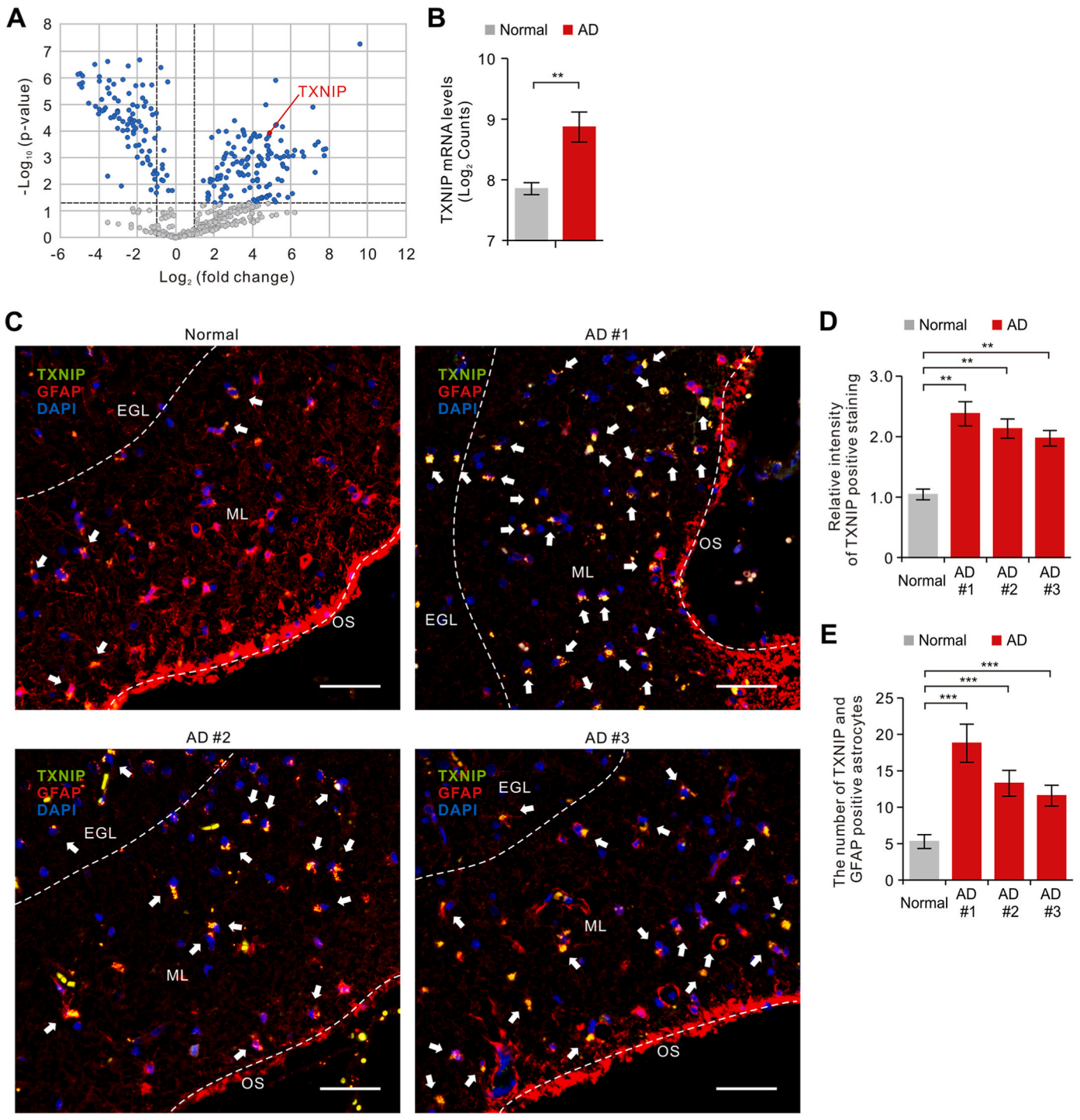

Fig. 1. The levels of TXNIP are elevated in GFAP-positive reactive astrocytes of cortex from patients with AD. (A) Volcano plots from the cerebral cortex region of brain tissues from patients with AD (AD) (n = 3) or non-AD (normal) (n = 3) in nanostring nCounter gene expression analysis. Volcano plots showing log2 fold change (x-axis) and -log10 *p*-values (y-axis) comparing patients with AD (AD) and non-AD (normal). Red dot represents TXNIP gene. Blue dots represent differentially expressed genes with *p*-value <0.05. Gray dots represent differentially expressed genes with *p*-value higher than 0.05. (B) The mRNA levels of TXNIP (log2 counts) in patients with AD (AD) and non-AD (normal). Data are presented as mean ± SD. **, $p < 0.01$ by Student's two-tailed *t*-test. (C) Representative immunofluorescence images of TXNIP protein expression in GFAP-positive astrocytes of the cerebral cortex region from patients with AD (AD #1, AD #2, AD #3) or non-AD (normal) (n = 3 per group) showing TXNIP (green) and GFAP (red) around molecular layer (ML). DAPI-stained nuclei are shown in blue. OS, Outer surface; ML, Molecular layer; EGL, External granular layer. Scale bars, 20 μm. White arrows indicate TXNIP and GFAP-double positive cells. Symbols, which are expressed by white dotted line, indicate distinct area among OS, ML, and EGL. (D) Quantification of intensity for TXNIP-positive staining in GFAP-positive astrocytes from immunofluorescence images in the cerebral cortex region from patients with AD (AD #1, AD #2, AD #3) or non-AD (normal) (n = 10 images per individual subject). Data are presented as mean ± SD. **, $p < 0.01$ by Student's two-tailed *t*-test and analysis of variance (ANOVA). (E) Quantification of TXNIP and GFAP-double positive astrocytes from immunofluorescence images in the cerebral cortex region from patients with AD (AD #1, AD #2, AD #3) or non-AD (normal) (n = 10 images per individual subject). Data are presented as mean ± SD. ***, $p < 0.001$ by Student's two-tailed *t*-test and analysis of variance (ANOVA). (For interpretation of the references to color in this figure legend, the reader is referred to the Web version of this article.)

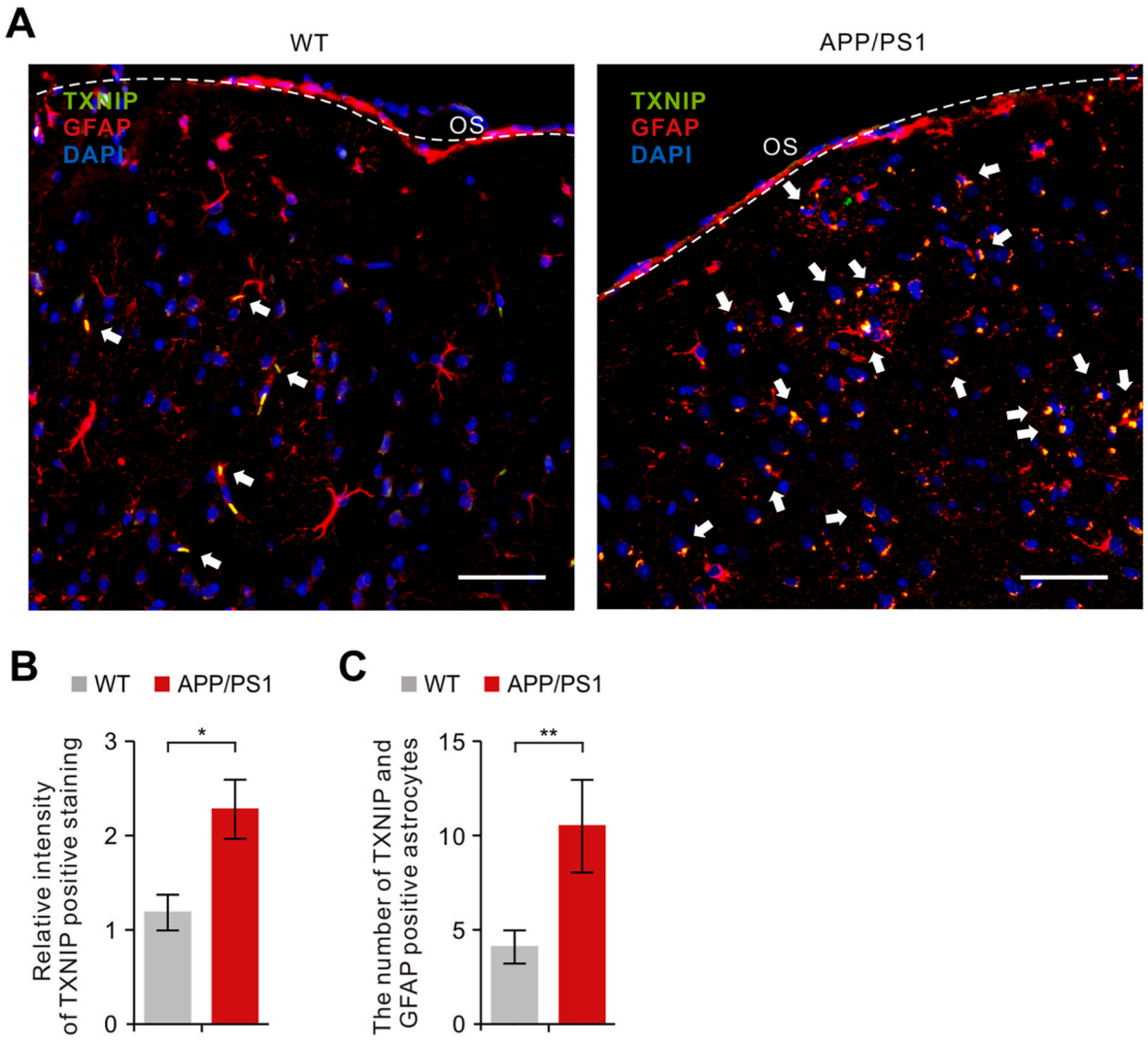

Fig. 2. The levels of TXNIP are elevated in GFAP-positive astrocytes of cortex from APP/PS1 mice. (A) Representative immunofluorescence images of TXNIP protein expression in GFAP- positive astrocytes of cerebral cortex region from brains of APP/PS1 mice (APP/PS1) or wild-type mice (WT) (n = 5 per group) showing TXNIP (green) and GFAP (red). DAPI-stained nuclei are shown in blue. Scale bar, 20 μm. White arrows indicate TXNIP and GFAP-double positive cells. OS, Outer surface. (B) Quantification of intensity for TXNIP-positive staining in GFAP-positive astrocytes from immunofluorescence images in the cerebral cortex region from brains of APP/PS1 mice (APP/PS1) or wild-type mice (WT) (total 10 images from n = 5 per group). Data are presented as mean ± SD. *, $p < 0.05$ by Student's two-tailed *t*-test. (C) Quantification of TXNIP and GFAP-double positive astrocytes from immunofluorescence images in the cerebral cortex region from brains of APP/PS1 mice (APP/PS1) or wild-type mice (WT) (total 10 images from n = 5 per group). Data are presented as mean ± SD. **, $p < 0.01$ by Student's two-tailed *t*-test. (For interpretation of the references to color in this figure legend, the reader is referred to the Web version of this article.)

that TXNIP increases pro-inflammatory phenotype in human astrocytes.

3.4. TXNIP increases mtROS production and decreases cellular antioxidant process in human astrocytes

Next, we investigated the underlying molecular mechanism by which TXNIP induces pro-inflammatory response in human astrocytes. Since mtROS play an important role in the inflammatory signaling, we investigated whether TXNIP could induce mtROS production in human astrocytes. We analyzed levels of mtROS production by TXNIP over-expression in human astrocytes (Fig. 4A). Over-expression of TXNIP significantly increased the production of mtROS relative to the control (Fig. 4A). We also investigated whether TXNIP could decrease cellular antioxidant process in human astrocytes. We measured the status of glutathione (GSH) and the ratio of reduced GSH to oxidized glutathione (GSSG) as an indicator of oxidative stress. Elevation of TXNIP significantly decreased levels of GSH and the ratio of GSH/oxidized glutathione (GSSG) compared to the control (Fig. 4B and C). Elevation of TXNIP also increased levels of GSSG relative to the control (Fig. 4D). Since TXNIP induced the reduction of GSH and the ratio GSH/GSSG, we analyzed whether TXNIP could regulate levels of nuclear factor erythroid 2–related factor 2 (NRF2) signaling pathway, a key regulator of the cellular antioxidant response, in human astrocytes. Elevation of TXNIP decreased levels of nuclear translocation of NRF2 relative to the control (Fig. 4E). Moreover, levels and activity of heme oxygenase-1 (HO-1) (Fig. 4F and G) and glutamate cysteine ligase (GCL) (Fig. 4H and I) as the target of NRF2 were significantly decreased by TXNIP over-expression in human astrocytes. These results suggest that TXNIP increases mtROS production and decreases cellular antioxidant process in human astrocytes.

3.5. TXNIP induces mitochondrial oxidative stress by reducing mitochondrial respiration and ATP production in human astrocytes

We investigated the underlying molecular mechanism by which TXNIP increases mitochondrial oxidative stress by mtROS production in

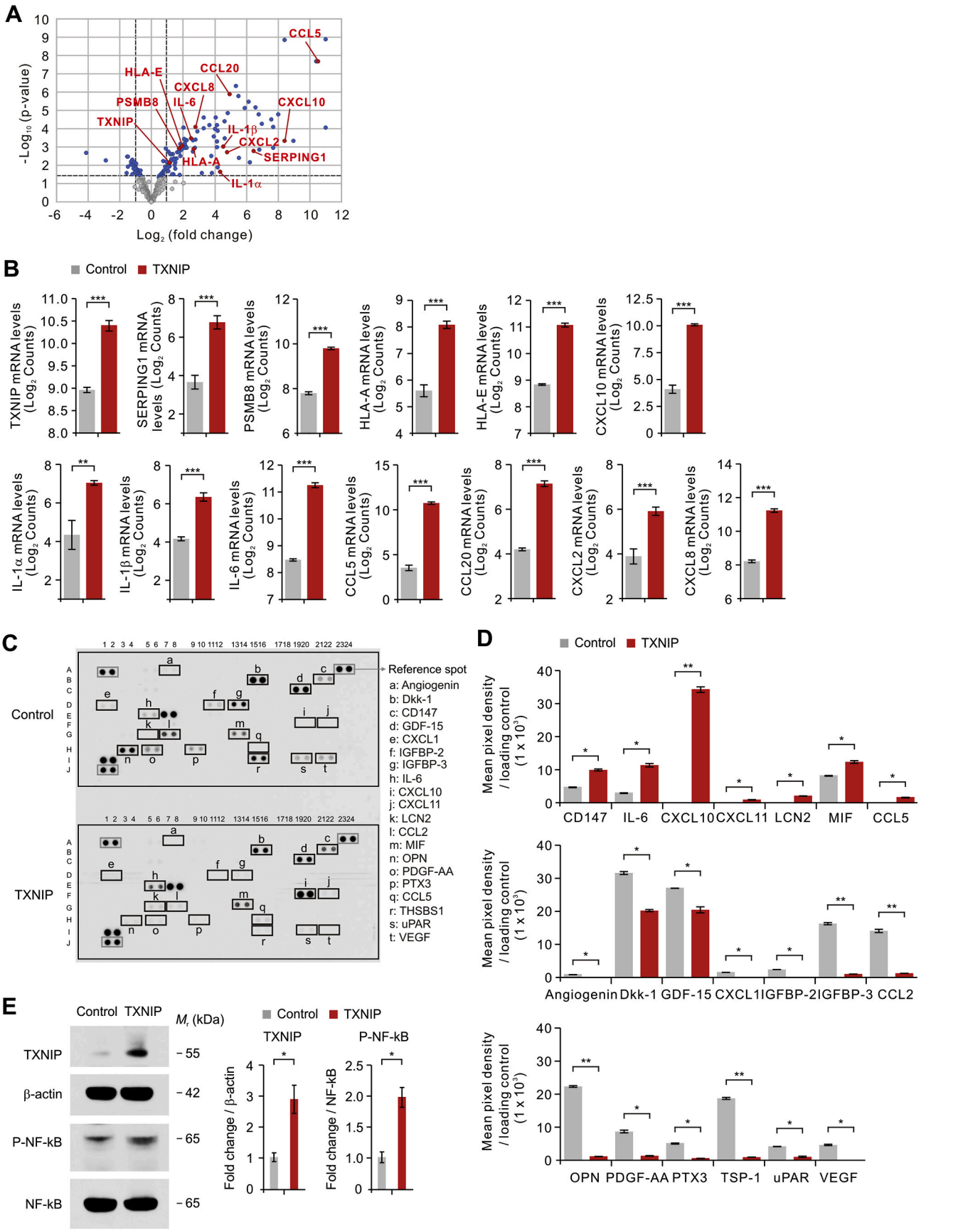

(caption on next page)

Fig. 3. TXNIP increases pro-inflammatory phenotype in human astrocytes. (A) Volcano plots from control (Control) (n = 3) and TXNIP overexpressing (TXNIP) (n = 3) human astrocytes in nanostring nCounter gene expression analysis. Volcano plots showing log2 fold change (x-axis) and -log10 *p*-values (y-axis) comparing control (Control) and TXNIP overexpressing (TXNIP) human astrocytes in nanostring nCounter gene expression analysis. Red dots represent TXNIP, SERPING1, PSMB8, HLA-A, HLA-E, CXCL10, IL-1α, IL-1β, IL-6, CCL5, CCL20, CXCL2 and CXCL8 gene. Blue dots represent differentially expressed genes with *p*-value <0.05. Gray dots represent differentially expressed genes with *p*-value higher than 0.05. (B) The mRNA levels of TXNIP, SERPING1, PSMB8, HLA-A, HLA-E, CXCL10, IL-1α, IL-1β, IL-6, CCL5, CCL20, CXCL2 and CXCL8 (log2 counts) in control (Control) and TXNIP overexpressing (TXNIP) human astrocytes. Data are presented as mean ± SD. **, $p < 0.01$; ***, $p < 0.001$ by Student's two-tailed *t*-test. (C) Representative images of multiple cytokines, chemokine, growth factors, and other soluble proteins in supernatants from control (Control) and TXNIP overexpressing (TXNIP) human astrocytes. The location of targets was indicated by the number of x-axis and the capital character of y-axis. The name of targets was indicated by a to t in right. (D) Quantification of pixel density for up-regulated targets (CD147, IL-6, CXCL10, CXCL11, LCN2, MIF, and CCL5) or down-regulated targets (Angiogenin, Dkk-1, GDF-15, CXCL1, IGFBP-2, IFGBP-3, CCL2, OPN, PDGF-AA, PTX3, TSP-1, uPAR, and VEGF) from D. Data are presented as mean ± SD. **, $p < 0.01$; *, $p < 0.05$ by Student's two-tailed *t*-test. (E) Representative immunoblot analysis for TXNIP and phosphorylated NF-kB in control (Control) and TXNIP overexpressing (TXNIP) human astrocytes. Quantification for protein levels of TXNIP and phosphorylated NF-kB in control (Control) and TXNIP overexpressing (TXNIP) human astrocytes. For immunoblots, β-actin and NF-kB were used as a loading control. Data are presented as mean ± SD. *, $p < 0.05$ using Student's two-tailed *t*-test. Data are representative of three independent experiments. (For interpretation of the references to color in this figure legend, the reader is referred to the Web version of this article.)

human astrocytes. We examined whether TXNIP could increase mitochondrial oxidative stress by reducing mitochondrial respiration and ATP production in human astrocytes. We analyzed oxygen consumption rate (OCR) as a parameter of mitochondrial respiration activity based on the quantification of oxygen consumption (Fig. 5A). The activity of mitochondrial respiration was measured by sequential addition of oligomycin (a selective inhibitor for mitochondrial respiration), FCCP (a potent uncoupler of mitochondrial oxidative phosphorylation), rotenone, and antimycin (specific inhibitors of mitochondrial Complex I and Complex III). Over-expression of TXNIP significantly decreased basal OCR levels compared to the control (Fig. 5A and B). Moreover, the levels of OCR in response to oligomycin and FCCP were significantly reduced by TXNIP over-expression relative to the control (Fig. 5A and B). Consistent with OCR levels, the production of mitochondrial ATP was significantly reduced by TXNIP over-expression compared to that in the control (Fig. 5C). Next, we investigated the molecular target in the regulation of mitochondrial respiration and ATP production by TXNIP elevation in human astrocytes. We analyzed levels of five protein complexes in mitochondrial ETC, including NADH:Ubiquinone Oxidoreductase Subunit B8 (NDUFB8) for Complex I, succinate dehydrogenase complex iron sulfur subunit B (SDHB) for Complex II, ubiquinol-cytochrome c reductase core protein 2 (UQCRC2) for Complex III, mitochondrially encoded cytochrome *c* oxidase I (MTCO1) for Complex IV, and ATP synthase F1 subunit alpha (ATP5F1A) for Complex V known to be critical enzymes for mitochondrial respiration and ATP production in human astrocytes (Fig. 5D). The elevation of TXNIP significantly decreased protein levels of Complex I (NDUFB8), Complex II (SDHB), Complex III (UQCRC2), Complex IV (MTCO1), and Complex V (ATP5F1A) enzyme relative to the control (Fig. 5D). These results suggest that TXNIP induces mitochondrial oxidative stress by reducing mitochondrial respiration and ATP production in human astrocytes.

3.6. Elevated TXNIP levels are correlated with caspase-3 activation in GFAP-positive astrocytes of cortex from patients with AD and APP/PS1 mice

Since mitochondrial oxidative stress is linked to caspase activation and apoptosis, we investigated whether elevated TXNIP levels could be correlated with caspase-3 activation of astrocytes during AD. We analyzed the protein levels of TXNIP and cleaved-caspase-3, an active form of caspase-3, in GFAP-positive astrocytes of cerebral cortex tissues from patients with AD (AD) or non-AD donor (Normal) (Fig. 6A and S3). The intensity of cleaved-caspase-3-positive staining was elevated in GFAP-positive astrocytes of cerebral cortex from patients with AD relative to that in non-AD donor (normal) (Fig. 6A and B and S3). Notably, the number of GFAP-positive astrocytes with positive subcellular co-localization between TXNIP and cleaved-caspase-3 was significantly increased in patients with AD (AD) compared to that in non-AD donor (normal) (Fig. 6A and C). Consistently, the intensity of cleaved-caspase-3-positive staining was elevated in GFAP-positive astrocytes of the cortex region of APP/PS1 mice compared to that in WT mice (Fig. 6D and E and S4). Moreover, the number of GFAP-positive astrocytes with positive subcellular co-localization between TXNIP and cleaved-caspase-3 was significantly increased in APP/PS1 mice compared to that in WT mice (Fig. 6D and F). These results suggest that elevated TXNIP levels are correlated with caspase-3 activation in GFAP-positive astrocytes of cortex from patients with AD and APP/PS1 mice.

3.7. TXNIP induces caspase-3 activation and mitochondria-dependent apoptosis in human astrocytes

We investigated whether elevation of TXNIP could induce caspase-3 activation and mitochondria-dependent apoptosis in human astrocytes. Since TXNIP induced mitochondrial oxidative stress in human astrocytes, we analyzed morphological impairment of mitochondria caused by TXNIP over-expression through immunofluorescence staining with Tomm20, an outer mitochondrial membrane protein (Fig. 7A). The elevation of TXNIP increased fragmentation of mitochondria relative to the control (Fig. 7A). The number of cells showing fragmentation of mitochondria was also significantly increased by TXNIP elevation compared to that in the control (Fig. 7B). Next, we analyzed morphological changes of cytotoxicity caused by TXNIP elevation in human astrocytes using a 3D analyzer (Fig. 7C). The elevation of TXNIP induced morphological features of cytotoxicity including shrinkage of cytosolic area and blebbing compared to the control (Fig. 7C). Moreover, the number of morphological dead cells caused by TXNIP elevation was significantly increased relative to the control (Fig. 7D). Consistent with results of morphological analysis, the elevation of TXNIP significantly increased levels of cytotoxicity compared to the control (Fig. 7E). Notably, the levels of cytochrome *c* in the cytosolic faction were significantly increased by TXNIP elevation compared to the control (Fig. 7F). Cytochrome *c* release from mitochondria were increased by TXNIP elevation relative to the control (Fig. 7F). Moreover, the activity of caspase-9 as an initiator caspase for mitochondria-dependent apoptosis was significantly increased by the elevation of TXNIP compared to the control (Fig. 7G). Consistently, the activity of caspase-3, an effector caspase for apoptosis, was significantly increased by the elevation of TXNIP relative to the control (Fig. 7H). These results suggest that TXNIP induces caspase-3 activation and mitochondria-dependent apoptosis in human astrocytes.

4. Discussion

Here we demonstrated that TXNIP contributes to induction of pro-inflammatory phenotype and caspase-3 activation in astrocytes during AD. We found that TXNIP levels are elevated in GFAP-positive astrocytes of cortex from human and mouse AD. We showed that TXNIP increased expression of genes related to pro-inflammatory phenotype, pro-inflammatory cytokines, and chemokines in human astrocytes. TXNIP also increased production of pro-inflammatory cytokines and

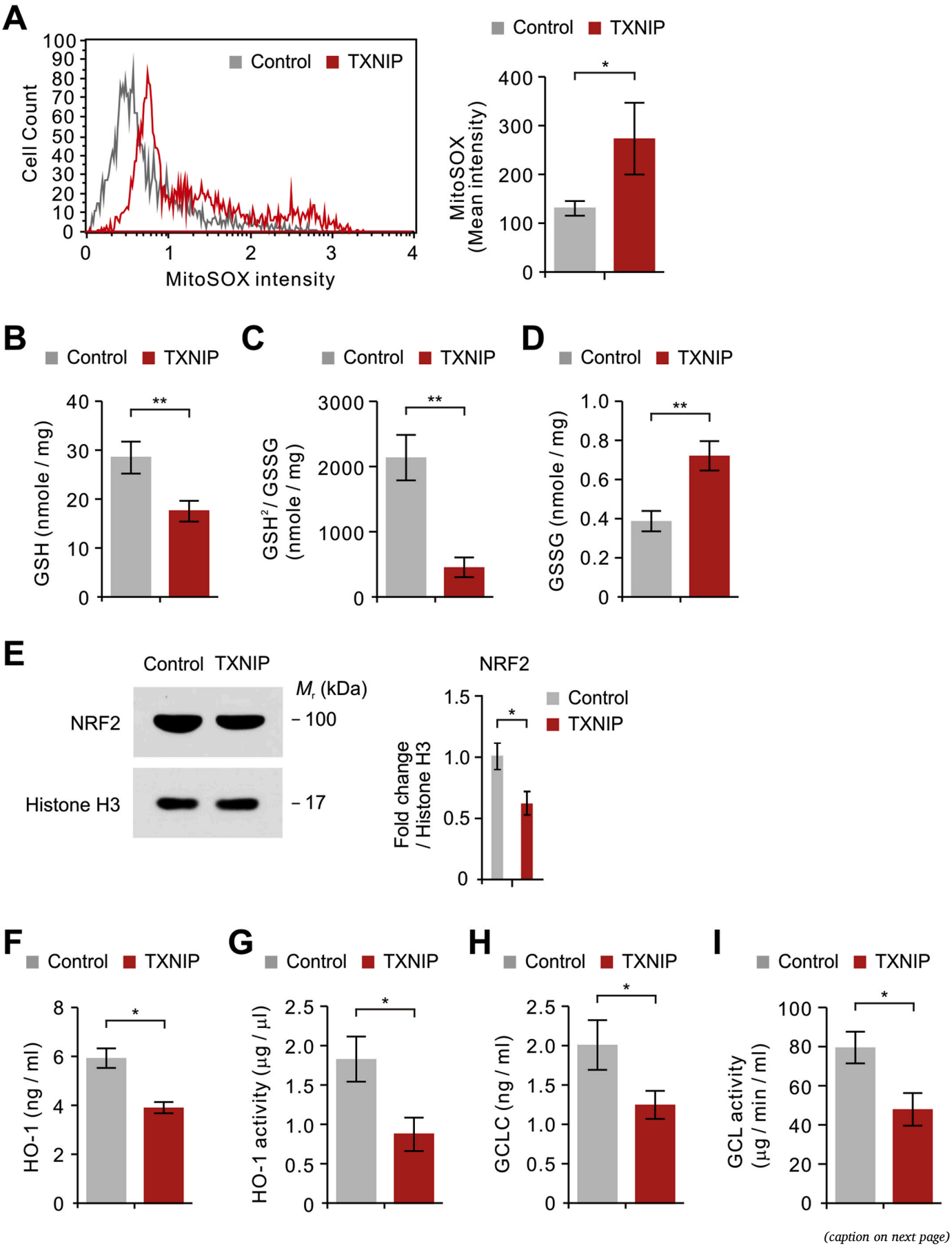

(caption on next page)

Fig. 4. TXNIP increases mtROS production and decreases cellular antioxidant process in human astrocytes. (A) Quantification of mtROS levels using MitoSOX staining in control (Control) and TXNIP overexpressing (TXNIP) human astrocytes. Data are presented as mean ± SD. *, $p < 0.05$ using two-tailed Student's t-test. (B–D) Quantification of (B) reduced GSH levels, (C) ratio of GSH^2/GSSG, and (D) GSSG levels in control (Control) and TXNIP overexpressing (TXNIP) human astrocytes. Data are presented as mean ± SD. **, $p < 0.01$ by Student's two-tailed *t*-test. (E) Representative immunoblot analysis for nuclear NRF2 in control (Control) and TXNIP overexpressing (TXNIP) human astrocytes. For immunoblots, histone H3 was used as a loading control. Data are presented as mean ± SD. *, $p < 0.05$ using two-tailed Student's t-test. (F–I) Quantification of (F) HO-1 protein levels, (G) HO-1 activity, (H) GCLC protein levels, and (I) GCL activity in control (Control) and TXNIP overexpressing (TXNIP) human astrocytes (n = 3 replicates per group). Data are presented as mean ± SD. *, $p < 0.05$ by Student's two-tailed *t*-test. Data are representative of three independent experiments.

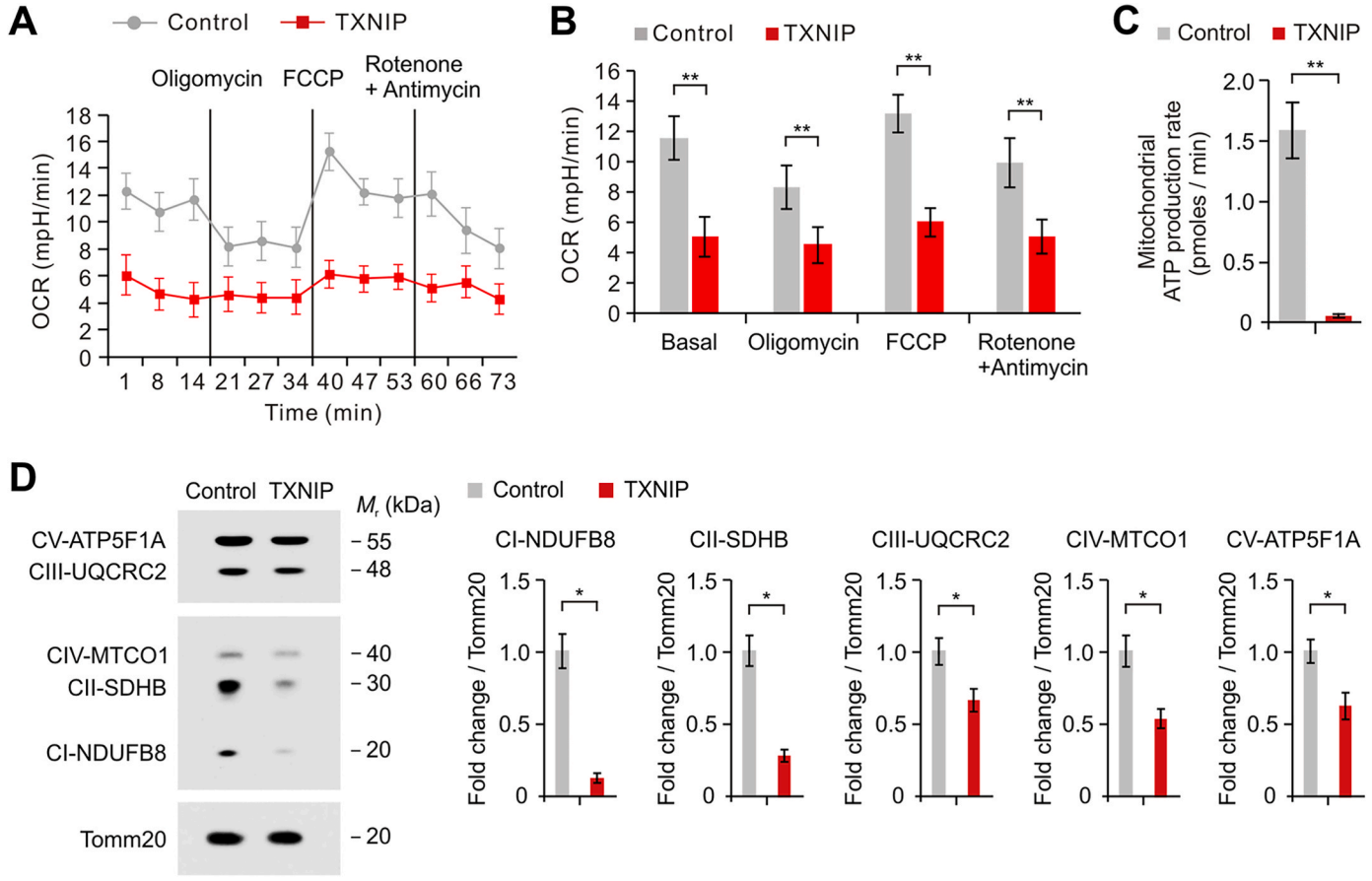

Fig. 5. TXNIP induces mitochondrial oxidative stress by reducing mitochondrial respiration and ATP production in human astrocytes. (A–B) Levels of oxygen consumption rate (OCR) (A) and quantification of OCR levels (B) in control (Control) and TXNIP overexpressing (TXNIP) human astrocytes (n = 3 replicates per group). Data are presented as mean ± SEM. **, $p < 0.01$ using two-tailed Student's t-test. (C) Quantification of mitochondrial ATP production rate in control (Control) and TXNIP overexpressing (TXNIP) human astrocytes (n = 3 replicates per group). Data are presented as mean ± SD. **, $p < 0.01$ using a two-tailed Student's t-test. (D) Representative immunoblot analysis for five mitochondrial ETC protein levels (left) including NDUFB8 for Complex I (C I (NDUFB8)), SDHB for Complex II (C II (SDHB)), UQCRC2 for Complex III (C III (UQCRC2)), MTCO1 for Complex IV (C IV (MTCO1)), and ATP5F1A for Complex V (C V (ATP5F1A)) in control (Control) and TXNIP overexpressing (TXNIP) human astrocytes. Quantification for protein levels of C I (NDUFB8), C II (SDHB), C III (UQCRC2), C IV (MTCO1), and C V (ATP5F1A) (right) in control (Control) and TXNIP overexpressing (TXNIP) human astrocytes. For immunoblots, Tomm20 was used as a loading control for mitochondrial protein. Data are presented as mean ± SD. *, $p < 0.05$ using two-tailed Student's t-test. Data are representative of three independent experiments.

chemokines in human astrocytes. We showed that TXNIP induced activation of NK-kB signaling and production of mtROS in human astrocytes. We found that elevated TXNIP levels are associated with caspase-3 activation in GFAP-positive astrocytes of cortex from human and mouse AD. We showed that TXNIP induced caspase-3 activation and mitochondria-dependent apoptosis in human astrocytes. Our findings suggest that TXNIP can be an upstream regulator for induction of pro-inflammatory phenotype and caspase-3 activation in astrocytes during AD.

Recent studies reported that the diverse heterogeneity and distinct molecular states of astrocytes by transcriptomic profiling in different disease models [25,43,44]. Astrocytes can be polarized into the pro-inflammatory, neurotoxic A1 reactive astrocytes after exposure to specific cytokines including tumor necrosis factor (TNF)-α, IL-1α, and complement component 1q (C1q) secreted by microglia exposed to lipopolysaccharide (LPS), whereas astrocytes can acquire a neuroprotective phenotype in the middle cerebral arterial occlusion (MCAO) model of ischemic stroke [25,43,44]. Our results found that elevation of TXNIP increased expression of genes related to pro-inflammatory phenotype such as SERPING1 and PSMB8 and production of pro-inflammatory cytokines and chemokines including IL-6, CXCL10, CXCL11, and CCL5 in human astrocytes. Our results also found that TXNIP increased production of LCN2, a potent neurotoxic factor secreted from reactive astrocytes [45], in human astrocytes. As an upstream signaling of the regulation of inflammatory cytokines and chemokines by TXNIP over-expression, our results found that TXNIP

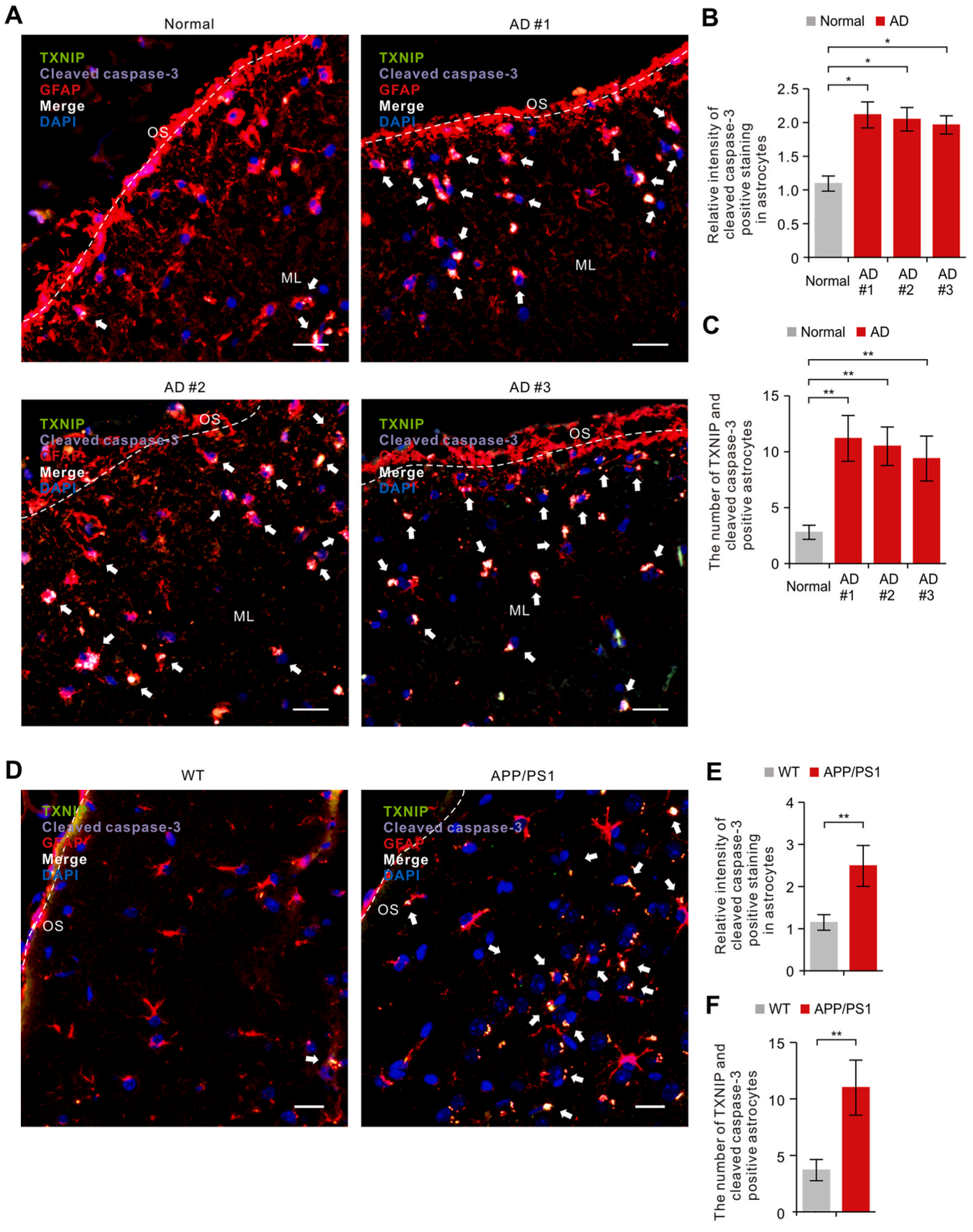

(caption on next page)

Fig. 6. High levels of TXNIP are correlated with caspase-3 activation in GFAP-positive astrocytes of cortex from patients with AD and APP/PS1 mice. (A) Representative immunofluorescence images of TXNIP and cleaved-caspase-3 protein expression in the cerebral cortex tissues from patients with AD (AD #1, AD #2, AD #3) or non-AD (normal) (n = 3 per group) showing TXNIP (green) and cleaved-caspase-3 (purple) in GFAP (red)-positive astrocytes around molecular layer (ML). DAPI-stained nuclei are shown in blue. OS, Outer surface; ML, Molecular layer. Scale bars, 10 μm. White arrows indicate TXNIP and cleaved-caspase-3-double positive cells in GFAP-positive astrocytes. Symbols, which are expressed by white dotted line, indicate distinct area among OS and ML. (B) Quantification of intensity for cleaved-caspase-3-positive staining in GFAP-positive astrocytes from immunofluorescence images in the cerebral cortex region from patients with AD (AD) or non-AD (normal) (n = 10 images per individual subject). Data are presented as mean ± SD. *, $p < 0.05$ by Student's two-tailed *t*-test and analysis of variance (ANOVA). (C) Quantification of TXNIP and cleaved-caspase-3-double positive cells in GFAP-positive astrocytes from immunofluorescence images in the cerebral cortex region from patients with AD (AD) or non-AD (normal) (n = 10 images per individual subject). Data are presented as mean ± SD. **, $p < 0.01$ by Student's two-tailed *t*-test and analysis of variance (ANOVA). (D) Representative immunofluorescence images of TXNIP and cleaved-caspase-3 protein expression in the cerebral cortex region of brain from APP/PS1 mice (APP/PS1) or wild-type mice (WT) showing TXNIP (green) and cleaved-caspase-3 (purple) in GFAP (red)-positive astrocytes (n = 5 per group). DAPI-stained nuclei are shown in blue. Scale bar, 10 μm. White arrows indicate TXNIP and cleaved-caspase-3-double positive cells in GFAP-positive astrocytes. OS, Outer surface. Symbols, which are expressed by white dotted line indicates OS. (E) Quantification of intensity for cleaved-caspase-3-positive staining in GFAP-positive astrocytes from immunofluorescence images in the cerebral cortex region of APP/PS1 mice (APP/PS1) or wild-type mice (WT) (total n = 10 images from n = 5 per group). Data are presented as mean ± SD. **, $p < 0.01$ by Student's two-tailed *t*-test. (F) Quantification of TXNIP and cleaved-caspase-3-double positive cells in GFAP-positive astrocytes from immunofluorescence images in the cerebral cortex region of APP/PS1 mice (APP/PS1) or wild-type mice (WT) (total n = 10 images from n = 5 per group). Data are presented as mean ± SD. **, $p < 0.01$ by Student's two-tailed *t*-test. (For interpretation of the references to color in this figure legend, the reader is referred to the Web version of this article.)

induced the activation of NF-kB signaling in human astrocytes. Abnormal NF-κB activation has been implicated in AD [46]. NF-κB activation can induce expression and secretion of complement protein C3 in reactive astrocytes which can lead to the impairment of synaptic density and dendritic morphology [47]. Our results suggested that TXNIP may have a role in inducing pro-inflammatory astrocyte reactivity in astrocytes. Beside gain of inflammatory and toxic function in reactive astrocytes, reactive astrocytes lose their supportive role in the progression of neurodegenerative diseases [22,48]. Consistent with previous studies, our results showed that production of growth factors and neurotrophic factors such as GDF-15, OPN, PDGF-AA, TSP-1, uPAR, and VEGF was reduced by TXNIP over-expression in human astrocytes. Since the changes of MIF, PDGF-AA, uPAR, and VEGF by TXNIP over-expression are potentially relevant to TNF-α signaling pathway [49–52], further studies are needed to investigate the interaction between TXNIP and TNF-α signaling in the regulation of growth factors and neurotrophic factors in human astrocytes.

Among pro-inflammatory cytokines and chemokines which are elevated by TXNIP-overexpression in our results, IL-6, LCN2, CXCL10, and CXCL11 are implicated in the pathogenesis of AD. IL-6 contributes to early-stage amyloid plaque formation in human AD [53,54]. IL-6 signaling is linked to cognitive impairments and peripheral metabolic alterations in AD [55]. Chronic exposure of IL-6 to neurons can lead to neuronal death [56]. Plasma levels of LCN2 are elevated in mild cognitive impairment [57]. Levels of CXCL10 in cerebrospinal fluid (CSF) are positively correlated with cognitive impairment [58]. Exposure of CXCL10 can induce cell death in neurons [59]. CXCL11 can bind to CXCR3 receptor that induces Aβ plaque formation and behavioral deficits in APP/PS1 mouse model of AD [60]. Our results suggest that TXNIP can contribute to neuroinflammation by production of IL-6, LCN2, CXCL10, and CXCL11 in astrocytes during AD.

TXNIP contributes to mitochondrial dysfunction including mitochondrial membrane depolarization, fragmentation, and mitophagy [61,62]. Consistent with the previous studies, our results showed that TXNIP induced mitochondrial oxidative stress by over-production of mtROS and suppression of mitochondrial respiration and ATP production in human astrocytes. As a potential downstream event of TXNIP-induced mitochondrial oxidative stress, our results showed that TXNIP increased caspase-3 activation in human astrocytes. Our results also showed that elevated TXNIP levels are associated with caspsase-3 activation in human and mouse AD. We have previously reported that the elevation of NADPH oxidase 4 (NOX4) induced mitochondrial oxidative stress-mediated ferroptosis of astrocytes [16]. Since both TXNIP and NOX4 play a role in mitochondrial oxidative stress of astrocytes in our current or previous study, the interaction between TXNIP and NOX4 might be associated with caspase-3 activation of astrocytes. Further studies are needed to determine the role of interaction between TXNIP and NOX4 in caspase-3 activation of astrocytes during AD. In previous studies, caspase-3 has been implicated in the processing of amyloid precursor protein (APP) into amyloidogenic fragments and the accumulation of APP [63–65]. Caspase-3 has also been implicated in a mechanism for Aβ peptides promote neuronal pathological tau filament assembly by triggering caspase activation [66,67]. Our results suggest that TXNIP can contribute to caspase-3 activation in tau-mediated neurodegeneration as an upstream regulator during AD. Pathological modifications of tau including hyperphosphorylation and glycosylation are also crucial to the pathogenesis of neurofibrillary degeneration in AD [68]. The formation of NFTs is significantly correlated with the degree of cognitive impairment in AD [69]. NFTs can contribute to the inhibition of Complex I activity in mitochondrial ETC which suppresses mitochondrial respiration and ATP production [70]. However, the precise mechanism of NFTs formation is not completely understood yet. Our results showed that TNXIP suppressed mitochondrial respiration and ATP production via reduction of Complex I expression in human astrocytes. Regarding the upstream regulator of NFTs formation, our findings suggest that TNXIP may be involved in the formation or function of NFTs in astrocytes. Further study is needed to determine the role of TXNIP in the regulation of NFTs formation and function.

In our study, there is a potential limitation to this conclusion. It was difficult to obtain sex and age-matched post-mortem tissues from patients with AD or non-AD through the Netherlands Brain Bank in this study. Since both sex and age are different in post-mortem tissues from patients with AD or non-AD in this study, our study has a limitation to prove the role of TXNIP in the difference of sex and age during AD in human study. Further studies are needed to investigate the role of TXNIP using sex and age-matched post-mortem tissues in human study.

In summary, our study demonstrates that TXNIP contributes to induction of pro-inflammatory phenotype and caspase-3 activation in astrocytes as a molecular mechanism for the role of TXNIP in astrocytes during AD.

Author contributions

J.K., S.P. and J.-S.M. conceived the study. J.K. performed all experiments. J.L., I.D.Y., and J.K. performed experiments for IF images, 3D images, and nanostring analysis. J.L. performed cytotoxicity analysis. S. P. and J.K. performed mtROS production analysis. J.K., S.P. and J.-S.M. participated in data acquisition and interpretation of results. J.K., S.P. and J.-S.M. wrote the paper. J.-S.M. supervised the entire project. All authors read, revised, and approved the final manuscript.

Declaration of competing interest

The authors declare that they have no known competing financial

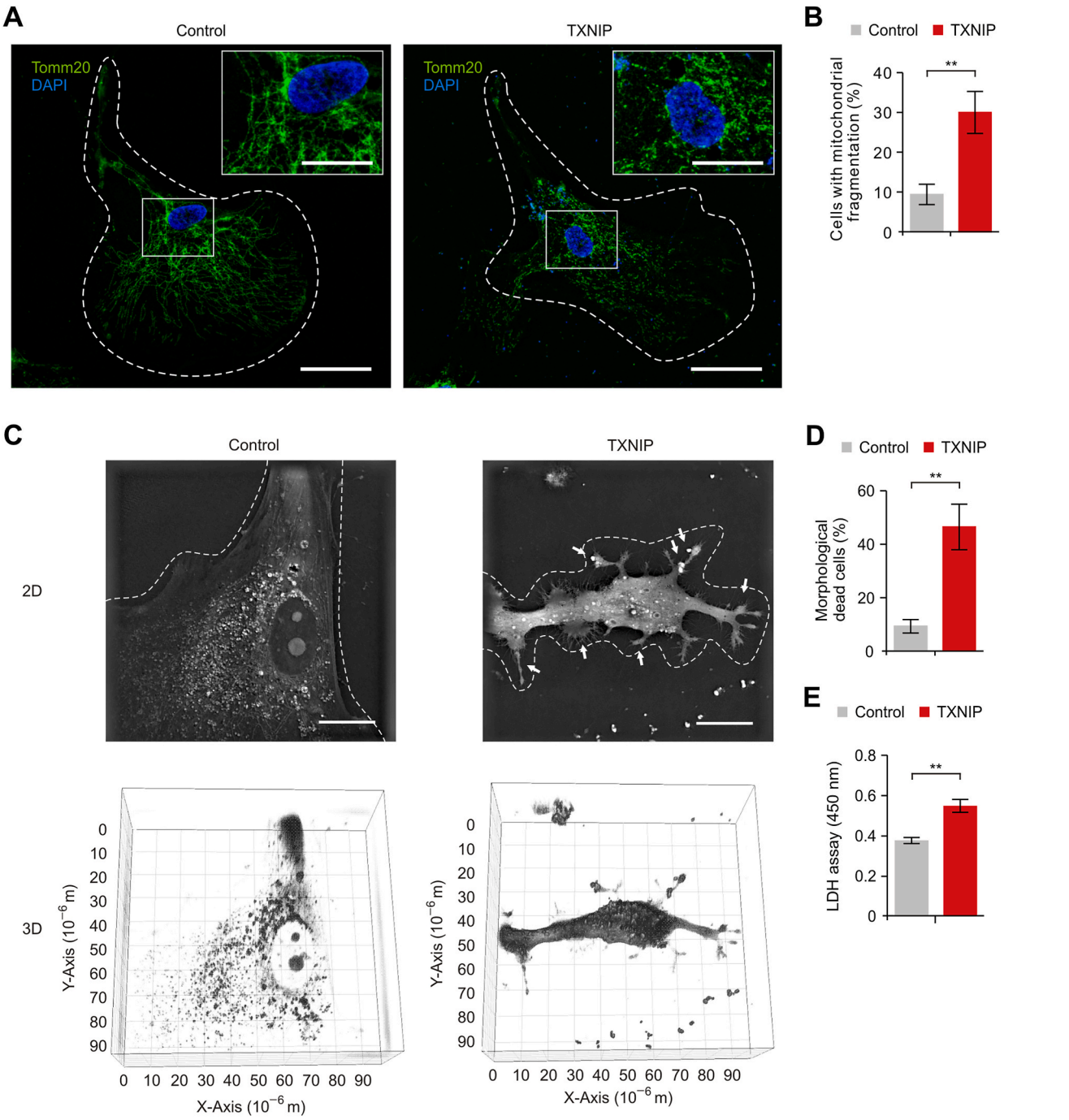

(caption on next page)

Fig. 7. TXNIP induces caspase-3 activation and mitochondria-dependent apoptosis in human astrocytes. (A) Representative immunofluorescence images of mitochondrial morphology for mitochondria fragmentation by outer mitochondrial membrane protein Tomm20 staining in control (Control) and TXNIP overexpressing (TXNIP) human astrocytes showing Tomm20 (green). DAPI-stained nuclei are shown in blue. Fragmentation of mitochondria is indicated (white arrows). Scale bar, 20 μm. Magnified views of selected regions (upper right): scale bar, 5 μm. (B) Quantification of cells with mitochondrial fragmentation from immunofluorescence images of mitochondrial morphology in control (Control) and TXNIP overexpressing (TXNIP) human astrocytes (The percent of morphological dead cells in a total of 100 cells from total n = 10 images per group from n = 3 replicates was calculated). Data are presented as mean ± SD. **, $p < 0.01$ using the two-tailed Student's t-test. (C) Representative 2D (top) and 3D (bottom) images of control (Control) and TXNIP overexpressing (TXNIP) human astrocytes (n = 10 images per group). Morphological features of cytotoxicity were indicated (white arrows). Scale bar, 20 μm. (D) Quantification of morphologically dead cells in control (Control) and TXNIP overexpressing (TXNIP) human astrocytes (The percent of morphologically dead cells in total 100 cells from total n = 10 images per group from n = 3 replicates was calculated). Data are presented as mean ± SD. **, $p < 0.01$ using two-tailed Student's t-test. (E) Cytotoxicity in control (Control) and TXNIP overexpressing (TXNIP) human astrocytes was determined based on LDH level. (F) Quantification of cytochrome *c* in cytosolic and mitochondrial fractions from control (Control) and TXNIP overexpressing (TXNIP) human astrocytes. Data are presented as mean ± SD. **, $p < 0.01$ using two-tailed Student's t-test. (G) Quantification of caspase-9 activity in control (Control) and TXNIP overexpressing (TXNIP) human astrocytes. Data are presented as mean ± SD. **, $p < 0.01$ using a two-tailed Student's t-test. (H) Quantification of caspase-3 activity in control (Control) and TXNIP overexpressing (TXNIP) human astrocytes. (n = 3 replicates per group). Data are presented as mean ± SD. **, $p < 0.01$ using the two-tailed Student's t-test. Data are representative of three independent experiments. (For interpretation of the references to color in this figure legend, the reader is referred to the Web version of this article.)

interests or personal relationships that could have appeared to influence the work reported in this paper.

Acknowledgements

This work was supported by National Research Foundation of Korea (NRF) grants (NRF-2021R1F1A1057801 to J.L., NRF-2022R1F1A1071128 to S.P., and NRF-2021R1C1C1007810 to J.-S.M.) and Soonchunhyang University Research Fund.

Appendix A. Supplementary data

Supplementary data related to this article can be found at https://doi.org/10.1016/j.redox.2023.102735.

References

[1] D.J. Selkoe, Alzheimer's disease: genes, proteins, and therapy, Physiol. Rev. 81 (2) (2001) 741–766, https://doi.org/10.1152/physrev.2001.81.2.741.
[2] M.T. Heneka, M.J. Carson, J. El Khoury, G.E. Landreth, F. Brosseron, D.L. Feinstein, A.H. Jacobs, T. Wyss-Coray, J. Vitorica, R.M. Ransohoff, K. Herrup, S.A. Frautschy, B. Finsen, G.C. Brown, A. Verkhratsky, K. Yamanaka, J. Koistinaho, E. Latz, A. Halle, G.C. Petzold, T. Town, D. Morgan, M.L. Shinohara, V.H. Perry, C. Holmes, N.G. Bazan, D.J. Brooks, S. Hunot, B. Joseph, N. Deigendesch, O. Garaschuk, E. Boddeke, C.A. Dinarello, J.C. Breitner, G.M. Cole, D.T. Golenbock, M. P. Kummer, Neuroinflammation in Alzheimer's disease, Lancet Neurol. 14 (4) (2015) 388–405, https://doi.org/10.1016/S1474-4422(15)70016-5.
[3] M.S. Buckwalter, T. Wyss-Coray, Modelling neuroinflammatory phenotypes in vivo, J. Neuroinflammation 1 (1) (2004) 10, https://doi.org/10.1186/1742-2094-1-10.
[4] B. Zhang, C. Gaiteri, L.G. Bodea, Z. Wang, J. McElwee, A.A. Podtelezhnikov, C. Zhang, T. Xie, L. Tran, R. Dobrin, E. Fluder, B. Clurman, S. Melquist, M. Narayanan, C. Suver, H. Shah, M. Mahajan, T. Gillis, J. Mysore, M. E. MacDonald, J.R. Lamb, D.A. Bennett, C. Molony, D.J. Stone, V. Gudnason, A. J. Myers, E.E. Schadt, H. Neumann, J. Zhu, V. Emilsson, Integrated systems approach identifies genetic nodes and networks in late-onset Alzheimer's disease, Cell 153 (3) (2013) 707–720, https://doi.org/10.1016/j.cell.2013.03.030.
[5] D.A. Butterfield, B. Halliwell, Oxidative stress, dysfunctional glucose metabolism and Alzheimer disease, Nat. Rev. Neurosci. 20 (3) (2019) 148–160, https://doi.org/10.1038/s41583-019-0132-6.
[6] W.J. Huang, X. Zhang, W.W. Chen, Role of oxidative stress in Alzheimer's disease, Biomed.Rep. 4 (5) (2016) 519–522, https://doi.org/10.3892/br.2016.630.
[7] D.A. Butterfield, J. Drake, C. Pocernich, A. Castegna, Evidence of oxidative damage in Alzheimer's disease brain: central role for amyloid beta-peptide, Trends Mol. Med. 7 (12) (2001) 548–554, https://doi.org/10.1016/s1471-4914(01)02173-6.
[8] W.R. Markesbery, Oxidative stress hypothesis in Alzheimer's disease, Free Radic. Biol. Med. 23 (1) (1997) 134–147, https://doi.org/10.1016/s0891-5849(96)00629-6.
[9] J.N. Peoples, A. Saraf, N. Ghazal, T.T. Pham, J.Q. Kwong, Mitochondrial dysfunction and oxidative stress in heart disease, Exp. Mol. Med. 51 (12) (2019) 1–13, https://doi.org/10.1038/s12276-019-0355-7.
[10] G. Ricci, L. Volpi, L. Pasquali, L. Petrozzi, G. Siciliano, Astrocyte-neuron interactions in neurological disorders, J. Biol. Phys. 35 (4) (2009) 317–336, https://doi.org/10.1007/s10867-009-9157-9.
[11] A. Rocchi, D. Valensin, C. Aldinucci, G. Giani, R. Barbucci, E. Gaggelli, H. Kozlowski, G. Valensin, NMR metabolomic investigation of astrocytes interacted with $A\beta_{42}$ or its complexes with either copper(II) or zinc(II), J. Inorg. Biochem. 117 (2012) 326–333, https://doi.org/10.1016/j.jinorgbio.2012.08.021.
[12] C.R. Figley, P.W. Stroman, The role(s) of astrocytes and astrocyte activity in neurometabolism, neurovascular coupling, and the production of functional neuroimaging signals, Eur. J. Neurosci. 33 (4) (2011) 577–588, https://doi.org/10.1111/j.1460-9568.2010.07584.x.
[13] T. Ishibashi, K.A. Dakin, B. Stevens, P.R. Lee, S.V. Kozlov, C.L. Stewart, R.D. Fields, Astrocytes promote myelination in response to electrical impulses, Neuron 49 (6) (2006) 823–832, https://doi.org/10.1016/j.neuron.2006.02.006.
[14] H. Phatnani, T. Maniatis, Astrocytes in neurodegenerative disease, Cold Spring Harbor Perspect. Biol. 7 (6) (2015), https://doi.org/10.1101/cshperspect.a020628.
[15] V. Karkkainen, J. Magga, J. Koistinaho, T. Malm, Brain environment and Alzheimer's disease mutations affect the survival, migration and differentiation of neural progenitor cells, Curr. Alzheimer Res. 9 (9) (2012) 1030–1042, https://doi.org/10.2174/156720512803569028.
[16] M.W. Park, H.W. Cha, J. Kim, J.H. Kim, H. Yang, S. Yoon, N. Boonpraman, S.S. Yi, I.D. Yoo, J.S. Moon, NOX4 promotes ferroptosis of astrocytes by oxidative stress-induced lipid peroxidation via the impairment of mitochondrial metabolism in Alzheimer's diseases, Redox Biol. 41 (2021), 101947, https://doi.org/10.1016/j.redox.2021.101947.
[17] D. Singh, Astrocytic and microglial cells as the modulators of neuroinflammation in Alzheimer's disease, J. Neuroinflammation 19 (2022), https://doi.org/10.1186/s12974-022-02565-0.
[18] C. Cordiglieri, C. Farina, Astrocytes Exert and control immune responses in the brain, CIR 6 (2010) 150–159, https://doi.org/10.2174/157339510791823655.
[19] C. Farina, F. Aloisi, E. Meinl, Astrocytes are active players in cerebral innate immunity, Trends Immunol. 28 (3) (2007) 138–145, https://doi.org/10.1016/j.it.2007.01.005.
[20] L. Ben Haim, M.-A. Carrillo-de Sauvage, K. Ceyzériat, C. Escartin, Elusive roles for reactive astrocytes in neurodegenerative diseases, Front. Cell. Neurosci. 9 (2015) 278, https://doi.org/10.3389/fncel.2015.00278.
[21] C. Escartin, O. Guillemaud, M.-A. Carrillo-de Sauvage, Questions and (some) answers on reactive astrocytes, Glia 67 (2019) 2221–2247, https://doi.org/10.1002/glia.23687.
[22] S.A. Liddelow, B.A. Barres, Reactive astrocytes: production, function, and therapeutic potential, Immunity 46 (2017) 957–967, https://doi.org/10.1016/j.immuni.2017.06.006.
[23] J.T. Hinkle, V.L. Dawson, T.M. Dawson, The A1 astrocyte paradigm: new avenues for pharmacological intervention in neurodegeneration, Mov. Disord. 34 (2019) 959–969, https://doi.org/10.1002/mds.27718.
[24] M. Neal, J. Luo, D.S. Harischandra, R. Gordon, S. Sarkar, H. Jin, V. Anantharam, L. Désaubry, A. Kanthasamy, A. Kanthasamy, Prokineticin-2 promotes chemotaxis and alternative A2 reactivity of astrocytes, Glia 66 (2018) 2137–2157, https://doi.org/10.1002/glia.23467.
[25] S.A. Liddelow, K.A. Guttenplan, L.E. Clarke, F.C. Bennett, C.J. Bohlen, L. Schirmer, M.L. Bennett, A.E. Münch, W.-S. Chung, T.C. Peterson, D.K. Wilton, A. Frouin, B. A. Napier, N. Panicker, M. Kumar, M.S. Buckwalter, D.H. Rowitch, V.L. Dawson, T. M. Dawson, B. Stevens, B.A. Barres, Neurotoxic reactive astrocytes are induced by activated microglia, Nature 541 (2017) 481–487, https://doi.org/10.1038/nature21029.
[26] J. Rose, C. Brian, A. Pappa, M.I. Panayiotidis, R. Franco, Mitochondrial metabolism in astrocytes regulates brain bioenergetics, neurotransmission and redox balance, Front. Neurosci. 14 (2020), 536682, https://doi.org/10.3389/fnins.2020.536682.
[27] D. Nolfi-Donegan, A. Braganza, S. Shiva, Mitochondrial electron transport chain: oxidative phosphorylation, oxidant production, and methods of measurement, Redox Biol. 37 (2020), 101674, https://doi.org/10.1016/j.redox.2020.101674.
[28] X. Wang, B. Su, L. Zheng, G. Perry, M.A. Smith, X. Zhu, The role of abnormal mitochondrial dynamics in the pathogenesis of Alzheimer's disease, J. Neurochem. 109 (Suppl 1) (2009) 153–159, https://doi.org/10.1111/j.1471-4159.2009.05867.x. Suppl 1.
[29] M. Manczak, B.S. Park, Y. Jung, P.H. Reddy, Differential expression of oxidative phosphorylation genes in patients with Alzheimer's disease: implications for early mitochondrial dysfunction and oxidative damage, NeuroMolecular Med. 5 (2) (2004) 147–162, https://doi.org/10.1385/NMM:5:2:147.
[30] R. Guo, S. Zong, M. Wu, J. Gu, M. Yang, Architecture of human mitochondrial respiratory megacomplex I(2)III(2)IV(2), Cell 170 (6) (2017) 1247–1257.e12, https://doi.org/10.1016/j.cell.2017.07.050.

[31] R.Z. Zhao, S. Jiang, L. Zhang, Z.B. Yu, Mitochondrial electron transport chain, ROS generation and uncoupling (Review), Int. J. Mol. Med. 44 (1) (2019) 3–15, https://doi.org/10.3892/ijmm.2019.4188.

[32] M.J. Morgan, Z.-G. Liu, Crosstalk of reactive oxygen species and NF-κB signaling, Cell Res. 21 (2011) 103–115, https://doi.org/10.1038/cr.2010.178.

[33] M. Herb, A. Gluschko, K. Wiegmann, A. Farid, A. Wolf, O. Utermöhlen, O. Krut, M. Krönke, M. Schramm, Mitochondrial reactive oxygen species enable proinflammatory signaling through disulfide linkage of NEMO, Sci. Signal. 12 (2019), https://doi.org/10.1126/scisignal.aar5926.

[34] H. El-Osta, M.L. Circu, Mitochondrial ROS and Apoptosis, 2016, pp. 1–23, https://doi.org/10.1007/978-3-319-42139-1_1.

[35] E. Junn, S.H. Han, J.Y. Im, Y. Yang, E.W. Cho, H.D. Um, D.K. Kim, K.W. Lee, P. L. Han, S.G. Rhee, I. Choi, Vitamin D3 up-regulated protein 1 mediates oxidative stress via suppressing the thioredoxin function, J. Immunol. 164 (12) (2000) 6287–6295, https://doi.org/10.4049/jimmunol.164.12.6287.

[36] O.N. Spindel, C. Yan, B.C. Berk, Thioredoxin-interacting protein mediates nuclear-to-plasma membrane communication: role in vascular endothelial growth factor 2 signaling, Arterioscler. Thromb. Vasc. Biol. 32 (5) (2012) 1264–1270, https://doi.org/10.1161/ATVBAHA.111.244681.

[37] A. Shah, L. Xia, H. Goldberg, K.W. Lee, S.E. Quaggin, I.G. Fantus, Thioredoxin-interacting protein mediates high glucose-induced reactive oxygen species generation by mitochondria and the NADPH oxidase, Nox4, in mesangial cells, J. Biol. Chem. 288 (10) (2013) 6835–6848, https://doi.org/10.1074/jbc.M112.419101.

[38] B.C. Berk, Novel approaches to treat oxidative stress and cardiovascular diseases, Trans. Am. Clin. Climatol. Assoc. 118 (2007) 209–214.

[39] J. Yoshioka, W.A. Chutkow, S. Lee, J.B. Kim, J. Yan, R. Tian, M.L. Lindsey, E. P. Feener, C.E. Seidman, J.G. Seidman, R.T. Lee, Deletion of thioredoxin-interacting protein in mice impairs mitochondrial function but protects the myocardium from ischemia-reperfusion injury, J. Clin. Invest. 122 (1) (2012) 267–279, https://doi.org/10.1172/jci44927.

[40] E. Yoshihara, S. Masaki, Y. Matsuo, Z. Chen, H. Tian, J. Yodoi, Thioredoxin/Txnip: redoxisome, as a redox switch for the pathogenesis of diseases, Front. Immunol. 4 (2014) 514, https://doi.org/10.3389/fimmu.2013.00514.

[41] Y. Wang, Y. Wang, V. Bharti, H. Zhou, V. Hoi, H. Tan, Z. Wu, P. Nagakannan, E. Eftekharpour, J.F. Wang, Upregulation of thioredoxin-interacting protein in brain of amyloid-beta protein precursor/presenilin 1 transgenic mice and amyloid-beta treated neuronal cells, J. Alzheimers. Dis. 72 (1) (2019) 139–150, https://doi.org/10.3233/JAD-190223.

[42] G. Paxinos, K.B. Franklin, Paxinos and Franklin's the Mouse Brain in Stereotaxic Coordinates, Academic press, 2019.

[43] J.L. Zamanian, L. Xu, L.C. Foo, N. Nouri, L. Zhou, R.G. Giffard, B.A. Barres, Genomic analysis of reactive astrogliosis, J. Neurosci. 32 (2012) 6391–6410, https://doi.org/10.1523/JNEUROSCI.6221-11.2012.

[44] P. Hasel, I.V.L. Rose, J.S. Sadick, R.D. Kim, S.A. Liddelow, Neuroinflammatory astrocyte subtypes in the mouse brain, Nat. Neurosci. 24 (2021) 1475–1487, https://doi.org/10.1038/s41593-021-00905-6.

[45] F. Bi, C. Huang, J. Tong, G. Qiu, B. Huang, Q. Wu, F. Li, Z. Xu, R. Bowser, X.-G. Xia, H. Zhou, Reactive astrocytes secrete lcn2 to promote neuron death, Proc. Natl. Acad. Sci. U. S. A. 110 (2013) 4069–4074, https://doi.org/10.1073/pnas.1218497110.

[46] B. Kaltschmidt, M. Uherek, B. Volk, P.A. Baeuerle, C. Kaltschmidt, Transcription factor NF-kappaB is activated in primary neurons by amyloid beta peptides and in neurons surrounding early plaques from patients with Alzheimer disease, Proc. Natl. Acad. Sci. U. S. A. 94 (1997) 2642–2647, https://doi.org/10.1073/pnas.94.6.2642.

[47] H. Lian, L. Yang, A. Cole, L. Sun, A.C.-A. Chiang, S.W. Fowler, D.J. Shim, J. Rodriguez-Rivera, G. Taglialatela, J.L. Jankowsky, H.-C. Lu, H. Zheng, NFκB-activated astroglial release of complement C3 compromises neuronal morphology and function associated with Alzheimer's disease, Neuron 85 (2015) 101–115, https://doi.org/10.1016/j.neuron.2014.11.018.

[48] K. Li, J. Li, J. Zheng, S. Qin, Reactive astrocytes in neurodegenerative diseases, Aging Dis. 10 (2019) 664–675, https://doi.org/10.14336/AD.2018.0720.

[49] M. Krauthausen, M.P. Kummer, J. Zimmermann, E. Reyes-Irisarri, D. Terwel, B. Bulic, M.T. Heneka, M. Müller, CXCR3 promotes plaque formation and behavioral deficits in an Alzheimer's disease model, J. Clin. Invest. 125 (2015) 365–378, https://doi.org/10.1172/JCI66771.

[50] B. Li, B. Wang, M. Chen, G. Li, M. Fang, J. Zhai, Expression and interaction of TNF-α and VEGF in chronic stress-induced depressive rats, Exp. Ther. Med. 10 (2015) 863–868, https://doi.org/10.3892/etm.2015.2641.

[51] M. Niiya, K. Niiya, T. Kiguchi, M. Shibakura, N. Asaumi, K. Shinagawa, F. Ishimaru, K. Kiura, K. Ikeda, H. Ueoka, M. Tanimoto, Induction of TNF-alpha, uPA, IL-8 and MCP-1 by doxorubicin in human lung carcinoma cells, Cancer Chemother, Pharmacology 52 (2003) 391–398, https://doi.org/10.1007/s00280-003-0665-1.

[52] E.J. Battegay, E.W. Raines, T. Colbert, R. Ross, TNF-alpha stimulation of fibroblast proliferation. Dependence on platelet-derived growth factor (PDGF) secretion and alteration of PDGF receptor expression, J. Immunol. 154 (1995) 6040–6047, https://doi.org/10.4049/jimmunol.154.11.6040.

[53] K. Miwa, S. Okazaki, M. Sakaguchi, H. Mochizuki, K. Kitagawa, Interleukin-6, interleukin-6 receptor gene variant, small-vessel disease and incident dementia, Eur. J. Neurol. 23 (2016) 656–663, https://doi.org/10.1111/ene.12921.

[54] M. Huell, S. Strauss, B. Volk, M. Berger, J. Bauer, Interleukin-6 is present in early stages of plaque formation and is restricted to the brains of Alzheimer's disease patients, Acta Neuropathol. 89 (1995) 544–551, https://doi.org/10.1007/BF00571510.

[55] N.M. Lyra e Silva, R.A. Gonçalves, T.A. Pascoal, R.A.S. Lima-Filho, E. de P. F. Resende, E.L.M. Vieira, A.L. Teixeira, L.C. de Souza, J.A. Peny, J.T.S. Fortuna, Pro-inflammatory interleukin-6 signaling links cognitive impairments and peripheral metabolic alterations in Alzheimer's disease, Transl. Psychiatry 11 (2021), https://doi.org/10.1038/s41398-021-01349-z.

[56] S.M. Conroy, V. Nguyen, L.A. Quina, P. Blakely-Gonzales, C. Ur, J.G. Netzeband, A. L. Prieto, D.L. Gruol, Interleukin-6 produces neuronal loss in developing cerebellar granule neuron cultures, J. Neuroimmunol. 155 (2004) 43–54, https://doi.org/10.1016/j.jneuroim.2004.06.014.

[57] J. Choi, H.-W. Lee, K. Suk, Increased plasma levels of lipocalin 2 in mild cognitive impairment, J. Neurol. Sci. 305 (2011) 28–33, https://doi.org/10.1016/j.jns.2011.03.023.

[58] N.P. Rocha, P.L. Scalzo, I.G. Barbosa, M.S. Souza, I.B. Morato, E.L.M. Vieira, P. P. Christo, A.L. Teixeira, H.J. Reis, Cognitive status correlates with CXCL10/IP-10 levels in Parkinson's disease, Parkinsons Dis. (2014), 903796, https://doi.org/10.1155/2014/903796, 2014.

[59] Y. Sui, L. Stehno-Bittel, S. Li, R. Loganathan, N.K. Dhillon, D. Pinson, A. Nath, D. Kolson, O. Narayan, S. Buch, CXCL10-induced cell death in neurons: role of calcium dysregulation, 23, https://doi.org/10.1111/j.1460-9568.2006.04631.x, 2006, 957–964.

[60] M. Krauthausen, M.P. Kummer, J. Zimmermann, E. Reyes-Irisarri, D. Terwel, B. Bulic, M.T. Heneka, M. Müller, CXCR3 promotes plaque formation and behavioral deficits in an Alzheimer's disease model, J. Clin. Invest. 125 (2015) 365–378, https://doi.org/10.1172/JCI66771.

[61] G. Saxena, J. Chen, A. Shalev, Intracellular shuttling and mitochondrial function of thioredoxin-interacting protein, J. Biol. Chem. 285 (2010) 3997–4005, https://doi.org/10.1074/jbc.M109.034421.

[62] T.S. Devi, T. Yumnamcha, F. Yao, M. Somayajulu, R.A. Kowluru, L.P. Singh, TXNIP mediates high glucose-induced mitophagic flux and lysosome enlargement in human retinal pigment epithelial cells. https://doi.org/10.1242/bio.038521, 2019.

[63] F.G. Gervais, D. Xu, G.S. Robertson, J.P. Vaillancourt, Y. Zhu, J. Huang, A. LeBlanc, D. Smith, M. Rigby, M.S. Shearman, E.E. Clarke, H. Zheng, L.H. Van Der Ploeg, S. C. Ruffolo, N.A. Thornberry, S. Xanthoudakis, R.J. Zamboni, S. Roy, D. W. Nicholson, Involvement of caspases in proteolytic cleavage of Alzheimer's amyloid-beta precursor protein and amyloidogenic A beta peptide formation, Cell 97 (1999) 395–406, https://doi.org/10.1016/S0092-8674(00)80748-5.

[64] D.C. Lu, S. Rabizadeh, S. Chandra, R.F. Shayya, L.M. Ellerby, X. Ye, G.S. Salvesen, E.H. Koo, D.E. Bredesen, A second cytotoxic proteolytic peptide derived from amyloid beta-protein precursor, Nat. Med. 6 (2000) 397–404, https://doi.org/10.1038/74656.

[65] M. Zhao, J. Su, E. Head, C.W. Cotman, Accumulation of caspase cleaved amyloid precursor protein represents an early neurodegenerative event in aging and in Alzheimer's disease, Neurobiol. Dis. 14 (2003) 391–403, https://doi.org/10.1016/j.nbd.2003.07.006.

[66] T.C. Gamblin, F. Chen, A. Zambrano, A. Abraha, S. Lagalwar, A.L. Guillozet, M. Lu, Y. Fu, F. Garcia-Sierra, N. LaPointe, R. Miller, R.W. Berry, L.I. Binder, V.L. Cryns, Caspase cleavage of tau: linking amyloid and neurofibrillary tangles in Alzheimer's disease, Proc. Natl. Acad. Sci. U. S. A. 100 (2003) 10032–10037, https://doi.org/10.1073/pnas.1630428100.

[67] J.-H. Cho, G.V.W. Johnson, Glycogen synthase kinase 3 beta induces caspase-cleaved tau aggregation in situ, J. Biol. Chem. 279 (2004) 54716–54723, https://doi.org/10.1074/jbc.M403364200.

[68] C.-X. Gong, F. Liu, I. Grundke-Iqbal, K. Iqbal, Post-translational modifications of tau protein in Alzheimer's disease, J. Neural. Transm. 112 (2005) 813–838, https://doi.org/10.1007/s00702-004-0221-0.

[69] M.N. Braskie, A.D. Klunder, K.M. Hayashi, H. Protas, V. Kepe, K.J. Miller, S.-C. Huang, J.R. Barrio, L.M. Ercoli, P. Siddarth, Plaque and tangle imaging and cognition in normal aging and Alzheimer's disease, Neurobiol. Aging 31 (2010) 1669–1678, https://doi.org/10.1016/j.neurobiolaging.2008.09.012.

[70] D.C. David, S. Hauptmann, I. Scherping, K. Schuessel, U. Keil, P. Rizzu, R. Ravid, S. Dröse, U. Brandt, W.E. Müller, Proteomic and functional analyses reveal a mitochondrial dysfunction in P301L tau transgenic mice, J. Biol. Chem. 280 (2005) 23802–23814, https://doi.org/10.1074/jbc.M500356200.